Optical and Electrical Properties of

Ce Doped Silicon Based Thin Films

Optical and Electrical Properties of Ce

Doped Silicon Based Thin Films

By

Yuxuan Gao

B.Eng.

A Thesis

Submitted to the School of Graduate Studies

in Partial Fulfillment of the Requirements

for the Degree

Master of Applied Science

McMaster University

MASTER OF APPLIED SCIENCE (2020)   MCMASTER UNIVERSITY

Department of Engineering Physics   Hamilton, Ontario

TITTLE: Optical and Electrical Properties of Ce Doped Silicon Based

Thin Films

AUTHOR: YUXUAN GAO, B.Eng., (Northwestern Polytechnical

University, Xi'an, China)

NUMBER OF PAGES: IX, 85

Abstract

Silicon oxide and silicon oxynitride thin films with in-situ cerium (Ce) doping were deposited using electron-cyclotron-resonance plasma enhanced chemical-vapor deposition (ECR-PECVD) on p-type silicon substrates. Oxygen was gradually substituted by nitrogen to produce SiO_xN_y thin films with different layer compositions. Refractive indices extracted from variable-angle spectroscopic ellipsometry (VASE) measurements classified the thin films into two main groups, SiO_x and SiO_xN_y. The thin film composition was studied by Rutherford Backscattering Spectrometry (RBS), verifying the gradual increase in nitrogen content.

Photoluminescence (PL) spectra of samples were obtained using a 375 nm laser diode as an excitation source. All samples were subjected to post-deposition annealing treatment for 1 hour at different temperatures varying from 800 to 1200 °C in both 95% N_2 and 5% H_2 and pure N_2 gas environment, to investigate the effect of hydrogen passivation on the PL irradiance. Samples subjected to annealing yielded considerably stronger blue/white PL emission than as-deposited ones, due to the formation of Ce-containing clusters at a temperature of 1200 °C. Optimum layer composition and annealing condition to produce SiO_xN_y thin films with maximized Ce^{3+} excitation efficiency were determined. Besides, the effect of hydrogen fluoride (HF) etching on PL

irradiance was studied, showing that an HF (1%) etching duration of 90 s yields the highest PL irradiance.

Electrical measurements were carried out for all Ce doped samples as preliminary work for light-emitting device fabrication. ITO and Al are coated as electrodes on the front side of the thin films and backside of the substrates, respectively, using a radio frequency (RF) magnetron sputtering system. I-V measurements were performed to investigate the carrier injection properties and the dominating mechanism of carrier conduction was determined.

Acknowledgements

First of all, I would like to thank my supervisor, Prof. Peter Mascher, for constant support, guidance, and encouragement since I joined his research group. He is an understandable, considerate and patient person who taught me the way to overcome academic difficulties. I am also grateful for the opportunities he generously provided to attend workshops and conferences.

I would also thank Dr. Zahra Khatami, who helped me with my academic questions and shared the experiment experience with me. I also want to express my special gratitude to Prof. Rafael Kleiman who encouraged me to pursue my passion and helped me at the beginning of my master's program.

I would also like to thank my colleagues in the research group during my graduate study. I want to thank Aysegul Abdelal, Dr. Jacek Wojcik and Jeremy Miller for the lab training and guidance at the beginning of my project. Victoria Jarvis and James Britten helped me with the XRD experiment and data process tutorial. I want to thank my college Fahmida Azmi for the scientific discussion and her help during the conference and workshop.

I will also thank Prof. Lyudmila Goncharova and Jack Hendriks in the Tandetron Laboratory at Western University (London, Ontario) for their assistance with RBS measurements. I want to thank Doris Stevanovic and Ross Anthony at the Center for Emerging Device Technologies (CEDT) for general

assistance in the cleanroom and lab equipment training. And I want to thank Timothy Lo for the generous help on the glove box and Jim Garrett for making the furnace end cap.

Last but not least, I want to express my heartfelt gratitude for my parents for their constant support, encouragement, and understanding through the entire journal of my graduate life.

Contents

List of Figures

List of Tables

1. Introduction

1.1 Background of silicon photonics

During the past half-century, silicon has become the most important material for the semiconductor industry. Since 1958, when Jack Kilby from Texas Instruments came up with the revolutionary Integrated Circuit (IC), wherein all the components of the circuit are completely integrated[1], the semiconductor industry has evolved with unprecedented speed. Nowadays, every single piece of personal device or equipment would not have such various functionalities without the invention of the IC. The complexity of ICs is growing exponentially in order to provide better performance and more diverse functionalities. As is anticipated by Moore's Law[2], the number of transistors on one chip doubles every two years.

Silicon is of great interest due to its compatibility with complementary metal-oxide-semiconductor (CMOS) technology. However, the silicon (Si) industry has met great difficulties imposed by the physical limitations of photolithography, where even the Extreme Ultra-violet (EUV) couldn't significantly reduce the line width due to it's fixed maximum resolution. Therefore, efforts have been spent on other directions to give more possibilities to Si microelectronics. Silicon photonics, which allows the realizations of high-speed and low-cost communications, giving more possibilities for data communication, optical sensing, and chip to chip interconnects, is one of these

exciting directions[3,4]. Figure 1 shows the revenue spent on silicon photonics from 2010 to 2017.
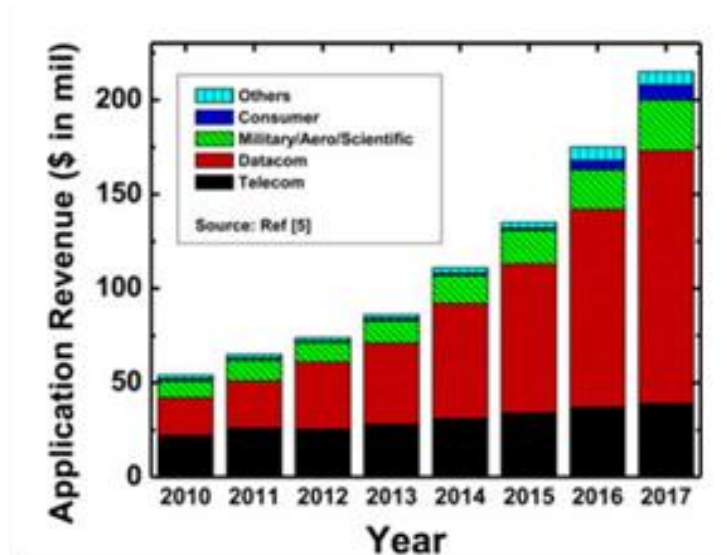
Figure 1. Silicon photonics application revenue from 2010 to 2017 [4].

By using waveguides on the chip instead of conventional metallic wires, silicon photonics is capable to overcome the bandwidth limitation and overheating problems[5]. However, most commercialized photonic devices are not compatible with the standard CMOS process, resulting in high cost, high complexity and low reliability in integration[6].

1.2 Light emission from silicon

By using Si-based materials including silicon oxide, silicon nitride, and silicon oxynitride, the cost for integration would drop significantly, due to their

2

compatibility with the highly developed CMOS process for mass production with high yield, thus boosting the development of the silicon photonics industry. Generating light from silicon has always been the most challenging part, due to the indirect bandgap of silicon limiting the efficiency of radiative recombination at room temperature. In order to excite an electron from the valance band to the conduction band, a phonon (lattice vibration) is required to fulfill the conservation of momentum. Therefore, the quantum efficiency of bulk silicon is less than 1%[7]. There are mainly two different approaches that can be used to obtain light with a higher quantum efficiency from silicon-based materials. One is to form silicon nanocrystals (Si-ncs) and the other is to dope rare-earth (RE) ions in the bulk materials. A detailed discussion of these two approaches can be found in the following sections.

1.2.1 Nanocrystals

Nanostructures are playing an important role in the optoelectronic research field and even in commercial products. It turns out that after intensive efforts spent on porous silicon, it is still challenging to obtain active light-emitting silicon-based devices. Besides, highly porous materials are vulnerable to standard CMOS technology[8]. Therefore, much attention has been transferred to Si-ncs to seek the new possibilities to achieve cost-effective and reliable light generation.

The Si-ncs light-emitting diode (LED) is able to emit red-NIR luminescence and its fabrication process can be integrated into CMOS line. The phenomena that light can be obtained from Si-ncs is defined as quantum

confinement (QC), which can be described by Heisenberg's uncertainty principle:

$$\Delta x \cdot \Delta p \geq \frac{\hbar}{2} \qquad (1.1)$$

Where the spatial uncertainty Δx times the momentum uncertainty Δp is no less than half of the reduced Planck's constant. As a consequence, in a Si-nc sample, the electron-hole pair will be confined spatially and gaining relatively large momentum, then the probability for radiative recombination will be greatly enhanced. The energy levels for the electrons can be calculated using a standard 'particle in the box' model[9]. Quantum dots (QDs) are the materials where quantum confinement occurs.
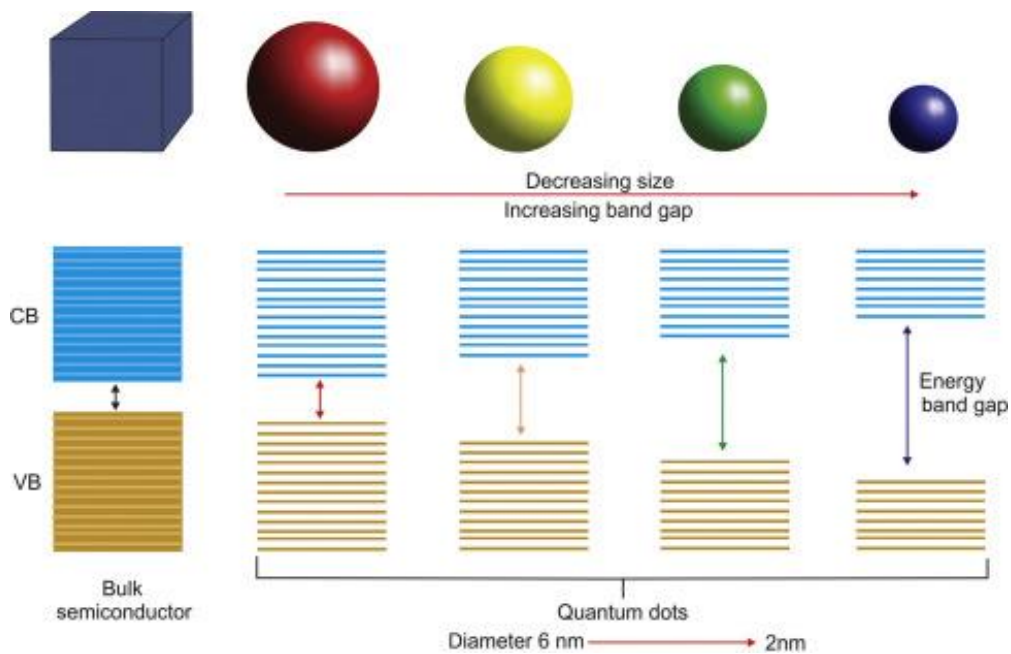
Figure 2. Energy band variation in quantum dots as the size is varied [10].

The bandgap of QDs can be tuned by controlling their size[10]. For instance, when QDs with an average size of 5 – 6 nm are excited by photons, orange/red emission can be obtained. QDs with smaller dimensions would emit light with shorter wavelengths because the bandgap will be increased with the decrease of QDs size. Figure 2 illustrates the relationship between QDs size and energy bandgap.

Si-ncs can be obtained by means of ion implantation into oxide layer[11], sputtering of Si-rich oxides[12], Molecular Beam Epitaxy (MBE)[13], and evaporation of Si oxide[14].

1.2.2 Rare earth (RE) ions

Another promising way to improve the electrical-optical conversion efficiency of silicon-based materials is to dope the materials with RE ions. The most common RE dopants are erbium (Er^{3+}), which can be used to produce infrared emission around 1550nm for optical communication applications, and europium (Eu^{3+}), terbium (Tb^{3+}) and cerium (Ce^{3+}) for RGB display.

Generally, RE ions all exhibit strong luminescence with a long lifetime (in the millisecond range) and narrow linewidths[15]. Different ions will yield different wavelengths from the visible to the near-infrared range. Figure 3 shows the energy levels of the triply charged RE ions.
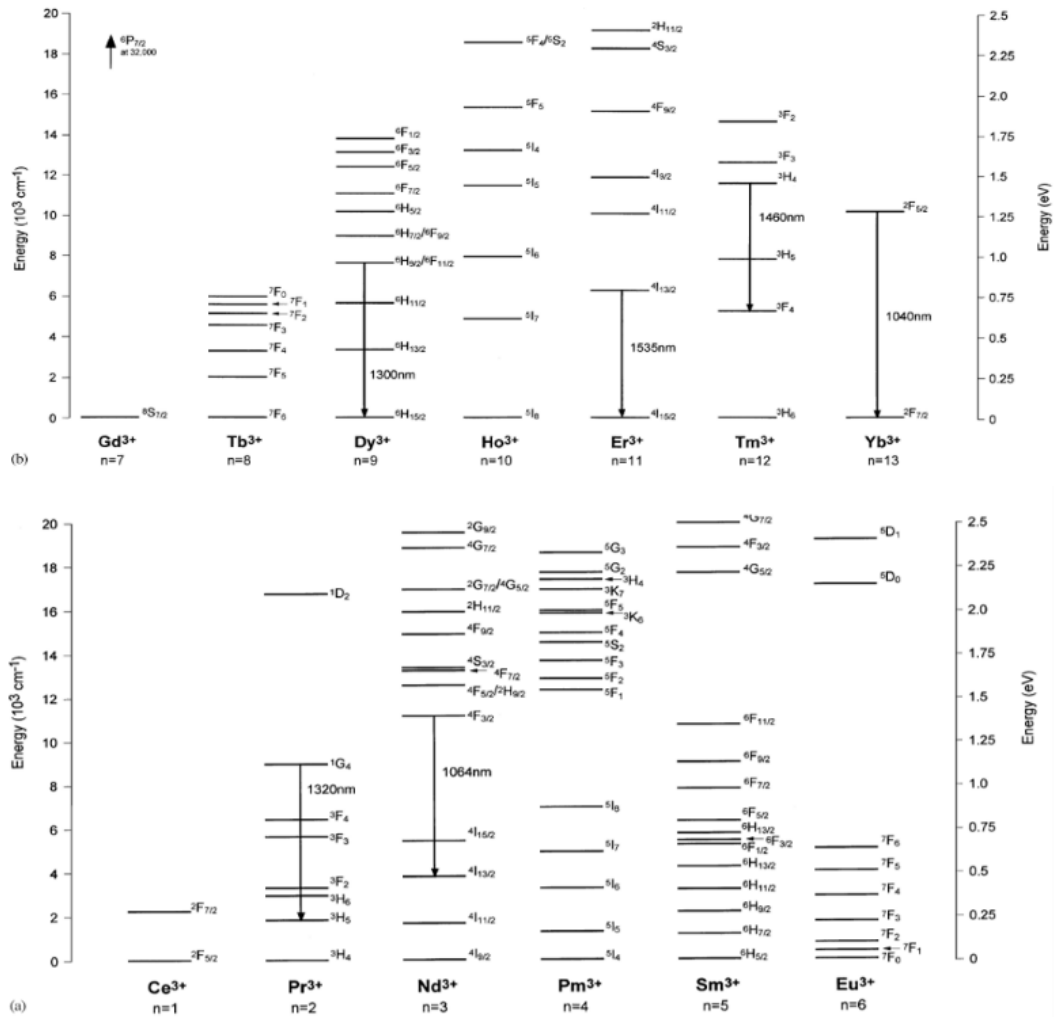
Figure 3. Energy levels of the triply charged RE ions. The most technologically important radiative transitions are labeled [15].

The mechanisms of RE luminescence in solid hosts generally can be classified into direct and indirect excitations. Direct excitations include resonant optical excitation from the interaction between photons, cathodoluminescence, and electroluminescence. Indirect mechanisms include carrier-mediated excitation transfer, and dipole-dipole Forster-Dexter coupling in insulators[15]. In

the carrier-mediated excitation mechanism, isoelectronic substitutional sites are occupied by RE elements, providing trap centers in which the free carriers interact with the partially filled 4f shell of the RE ion[15]. For example, Er^{3+} in gallium nitride will be excited to higher energy levels by free carriers and deexcited to lower levels with the assistance of photon coupling, emitting light at 523 nm. This mechanism is important for the fabrication of optoelectronic devices with good performance, however, the deep details of this mechanism still remain unknown.

Quenching effects will occur when the RE concentration is beyond a certain level. In this case, the ions will form either RE clusters or compounds/alloys with one component of the host matrix[15]. RE clusters will enhance the ion-ion interaction, quenching the luminescence. Compounds/alloys will also quench the luminescence due to their optical inactivity. For instance, the concentration limit for RE in solid hosts usually ranges from $7*10^{17}$ cm^{-3} to a few atomic percent.

Besides, phonon interactions will also limit the luminescence irradiance. Different electronic states will be connected by the phonons, depopulating the upper excited state, when a small number of phonons are presented[16]. Generally, if the phonon cut-off energy of the host is higher than a quarter of the energy gap of the transition where luminescence occurs, the quenching effect will occur. Consequently, the importance of multiphoton relaxation relies strongly on both the band diagram and the host matrix[15]. Take erbium, for example, the energy

of one of the emissions at 1535 nm is around 6500 cm^{-1}, while the phonon cut-off energy of silica is around 1100 cm^{-1}. So, the luminescence of erbium in silica is not strongly quenched. Therefore, host materials with low phonon energy such as Silica (1100 cm^{-1}) and Fluoride glass ZrF4 (400 – 600 cm^{-1}) are capable of reducing phonon interaction effects.

Interactions between RE ions is another factor which contributes to the loss of the irradiance of the luminescence[16] because these interactions will increase luminescence from undesired transitions, or the chance of non-radiative recombination.

1.2.3 Ce-doped silicon-based materials for luminescence

Ce ions can exist in silicon oxide with an oxidation state of either Ce^{3+} or Ce^{4+}, where Ce^{4+} has no 4f electron, making it optically inactive[5]. The luminescence properties of Ce^{3+} are governed by the transition between 5d-4f energy levels. The oscillator strength is stronger than the 4f-4f transitions due to the fact that the 5d-4f transition is partially allowed, making Ce^{3+} a brighter light emitter than other RE ions[5]. Besides, the luminescence properties of Ce^{3+} are also affected by the host matrix composition and post-deposition annealing (PDA)[17]. Typically, Ce nanostructures form by annealing cerium oxide layers deposited on silicon-based substrates at high temperatures. The $Ce_2Si_2O_7$ structure has demonstrated strong violet/blue luminescence at wavelengths in the 350 – 450

nm range[18,19]. luminescence from Ce_2SiO_5, $Ce_{9.33}[SiO_4]_6O_2$, and $CeSiO_4$, however, have not yet been reported due to the optical inactivity of Ce^{4+}.
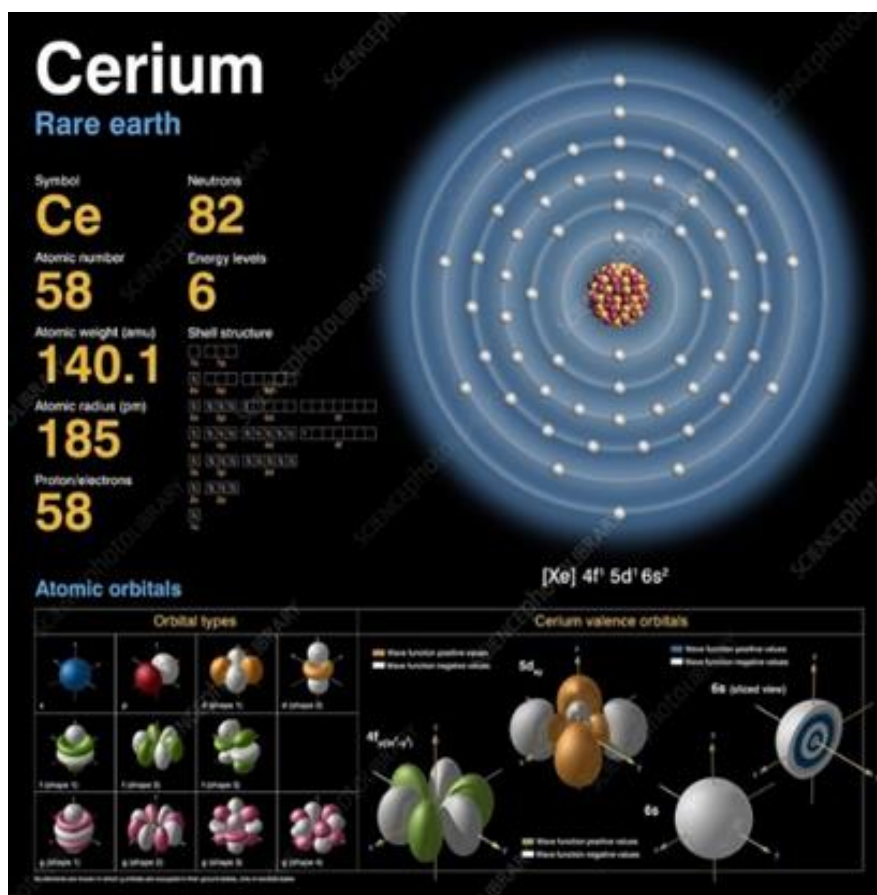
Figure 4. Atomic structure of cerium[20].

In 1998, Reisfeld et al. reported the spectroscopic properties of cerium in sol–gel glasses[21]. The majority composition of the glasses was silica (SiO_2) obtained by hydrolysis of ethoxy silane (TEOS). Blue luminescence was obtained from Ce^{3+} instead of the silica host with defects with a pumping laser at 337 nm. The emission from the silica host is broader and the decay time is shorter than that of Ce^{3+}.

In 2007, Xu et al. reported photoluminescence from Ce^{3+}-doped silica synthesized by sol–gel technique[22]. A broad luminescence band peaking at 445 nm was obtained with a pumping laser at 320 nm. The emission irradiance was enhanced with the increase of annealing temperature to 850 °C. The transitions from Ce^{4+} to Ce^{3+} during annealing was suggested to be the reason. Additionally, the decoration of S^{2-} and Cl^- anions can increase the luminescent irradiance and blue shift the luminescent wavelength. This was attributed to the phenomenon called nephelauxetic shift where the absorption and emission of Ce^{3+} would shift to longer wavelength with the increase of electronegativity of the surrounding ligands[21].
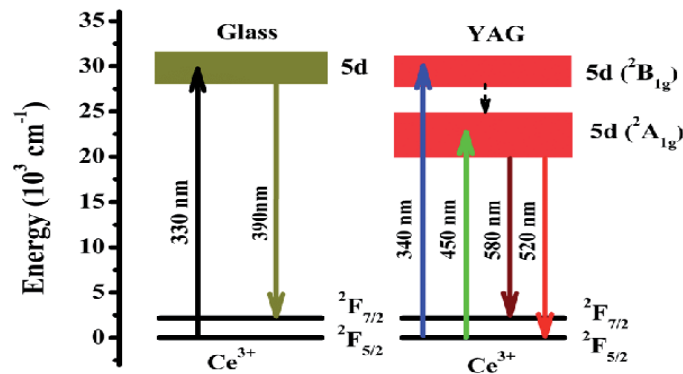
Figure 5. Energy level diagram of Ce 3+ with relative transitions in glass and in the YAG crystal[23].

However, the sol-gel technique suffers from drawbacks including porous final products, quenching of Ce^{3+} luminescence, and low solubility of Ce ions. In 2008, J. Li studied the luminescence of cerium doped silicon-rich silicon oxide (Ce-SRSO) and oxygen-rich silicon oxide (Ce-ORSO)[17]. In this work, different factors including the concentration of cerium ions, and different annealing conditions were studied to get the maximum luminescence. It was

found that the PL intensities of both samples are enhanced from 800°C, due to the Ce^{4+} - Ce^{3+} conversion and the reduction of oxide defects. More interestingly, when Ce-ORSO is annealed at 1200 °C, the irradiance of the PL gets greatly boosted. The author suggested this to be due to the formation of cerium clusters in the host matrix.

In 2012, P. Wilson studied the properties of Ce and Tb co-doped silicon oxide thin films[24]. Transmission electron microscopy, PL and synchrotron-based X-ray analysis were used to verify the presence of Ce-containing clusters after undergoing 1200 °C post-deposition annealing. Interestingly, the author found that the emission from Tb was increased significantly with the presence of Ce-containing clusters, which the author suggested to indicate that there was an energy transfer from Ce-containing clusters to Tb ions.

Later on, J. M. Ramírez continued the work and used different host materials including silicon oxides and silicon oxynitrides with Ce doping[25]. Different host material compositions and annealing temperatures were studied for both samples. The most intensive luminescence was obtained for both samples after annealing at 1180 °C, due to the formation of RE clusters.

1.3 Carrier transport in dielectric media

The study of the conduction mechanism in dielectric films and its application are significantly important to the microelectronics industry. In order to fabricate

a RE-doped light emitting device, one has to understand how charges are transported in dielectric media. Mechanisms of charge transport in dielectric materials have been intensively studied[26]. In a Metal–insulator–semiconductor (MIS) structure, the conductivity varies with different voltages applied and different temperatures. Figure 6 shows a typical structure of a RE doped light-emitting device, consisting of a 200 nm indium tin oxide (ITO) layer, 100 nm RE doped silicon oxide optically active layer, a p-type silicon substrate and 200 nm aluminum. ITO and aluminum act as anode and cathode, respectively for the device. The Fermi level of ITO is higher than the conduction band, so here we will consider ITO as metal in terms of conductivity[27]. The overall structure is considered as metal-insulator-semiconductor structure.
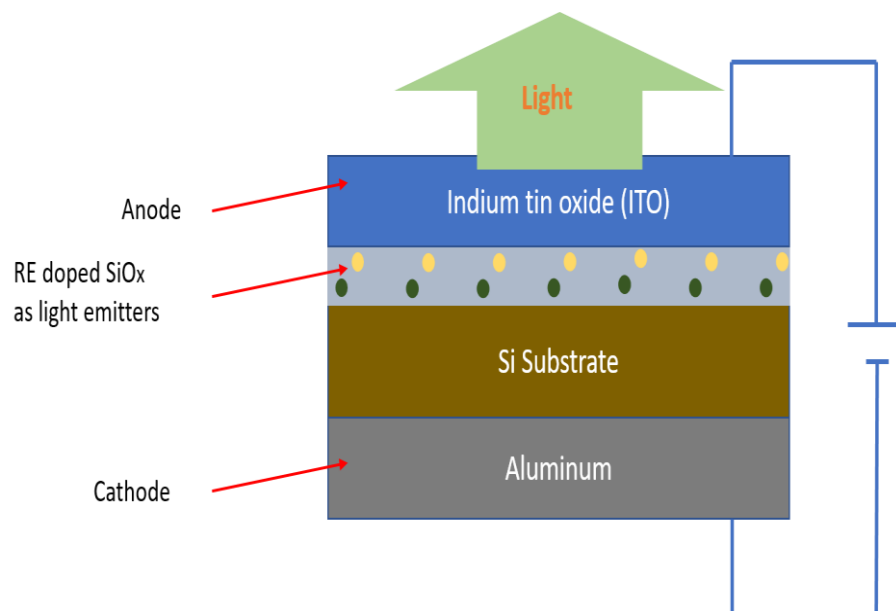
Figure 6. A MOS structured RE doped light emitting device.

Generally, charge transport mechanisms can be classified into two groups, electrode-limited current injection, and bulk-limited current injection[28]. Figure 7 shows the two categories of conduction mechanisms in dielectric films.
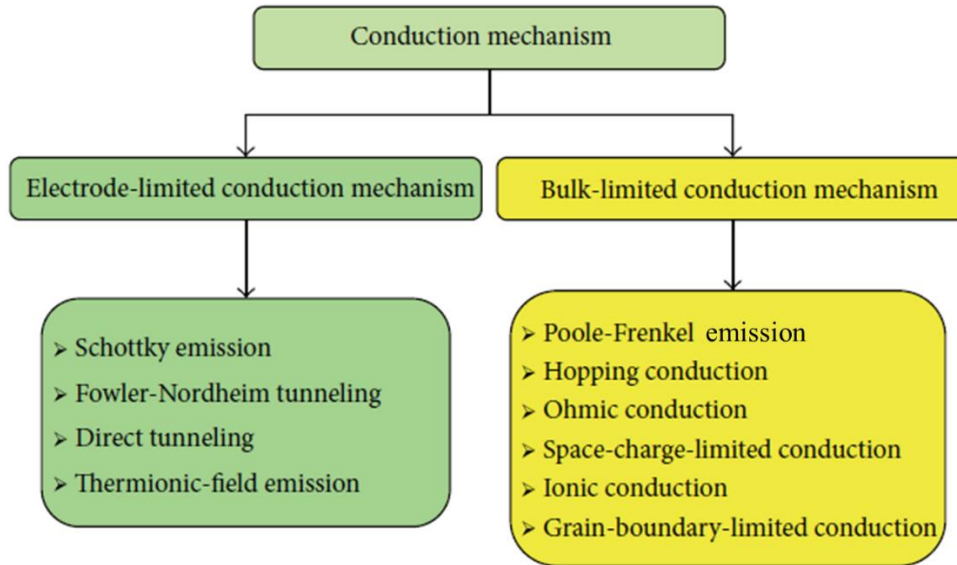
Figure 7. Classification of conduction mechanisms in dielectric films.

1.3.1 Electrode-limited conduction

In the electrode-limited conduction, the electrode-dielectric potential barrier is the main factor determining the number of injected carriers.

a). Schottky (thermionic) emission

Schottky emission is the process in which the electrons jump over the metal-dielectric energy barrier due to thermal excitation, which is one of the most commonly observed charge carrier transport mechanisms in dielectric films. Figure 8 illustrates the process of Schottky emission in an MIS band diagram.
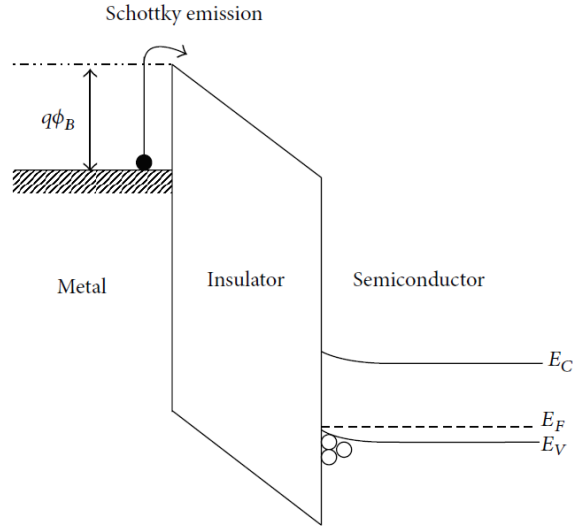
Figure 8. Illustration of Schottky emission in the energy band diagram.

The current density in Schottky emission can be written as:

$$J = A * T^2 \exp\left[\frac{-q\left(\phi_B - \sqrt{qE/4\pi\varepsilon_r\varepsilon_0}\right)}{kT}\right] \qquad (1.2)$$

$$A^* = \frac{4\pi\varepsilon k^2 m^*}{h^3} = \frac{120m^*}{m_0} \qquad (1.3)$$

Where J is the current density, A^* the effective Richardson constant, m_0 and m^* the electron mass and effective mass, respectively, T the absolute temperature, E the electric field across the dielectric, k the Boltzmann's constant, h the Planck's constant, ε_0 the permittivity in a vacuum, ε_r the material's dielectric constant, and ϕ_B the barrier potential. In the case of Schottky emission, according to Equation 1, the plot of $\log(J/T^2)$ versus $E^{1/2}$ should yield a linear curve.

b). Fowler-Nordheim (F-N) tunneling
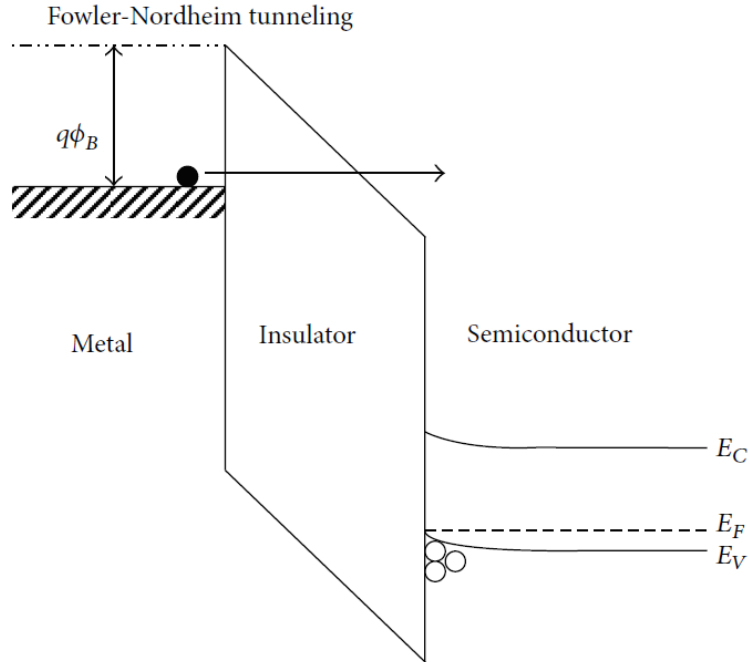
Figure 9. F-N tunneling mechanism.

The carriers will tunnel through the potential barrier if the dielectric film is thin enough (<10 nm) and a large electric field is applied. The current density for F-N tunneling is:

$$J = \frac{q^3 E^2}{8\pi h q \phi_B} \exp\left[\frac{-8\pi(2qm_T^*)^{\frac{1}{2}}}{3hE} \phi_B^{\frac{3}{2}}\right] \qquad (1.4)$$

Where m_T^* is the tunneling effective mass. This current can be extracted by measuring the I-V curve at low temperatures to eliminate the effect of thermionic emission. A plot of $\ln(J/E^2)$ versus $1/E$ should be linear in this case.

The mechanism of F-N tunneling is illustrated in figure 9.

c). Direct tunneling

Direct tunneling occurs before the applied voltage reaches the threshold of F-N tunneling. Direct tunneling becomes the dominant mechanism when the thickness of SiO_2 is less than around 3.5 nm. Figure 10 shows the mechanism of direct tunneling in an MIS structure.
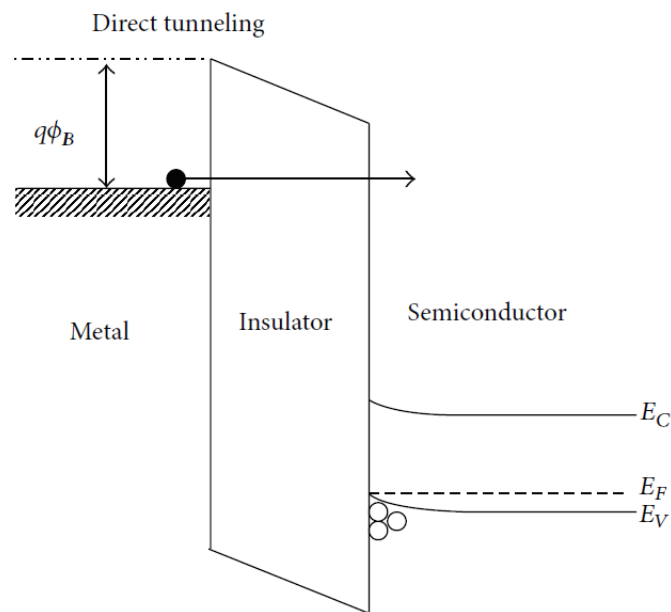
Figure 10. Mechanism of direct tunneling.

d). Thermionic-field emission

The thermionic-field emission mechanism is shown in figure 11. The energy of the electron in this case, is lower than for thermionic emission and higher than for field emission. The current density can be written as:

$$J = \frac{q^2 \sqrt{m} (kT)^{\frac{1}{2}} E}{8\hbar^2 \pi^{5/2}} \exp\left(-\frac{q\phi_0}{kT}\right) \exp\left[\frac{\hbar^z q^2 E^2}{24m(kT)^3}\right] \qquad (1.5)$$
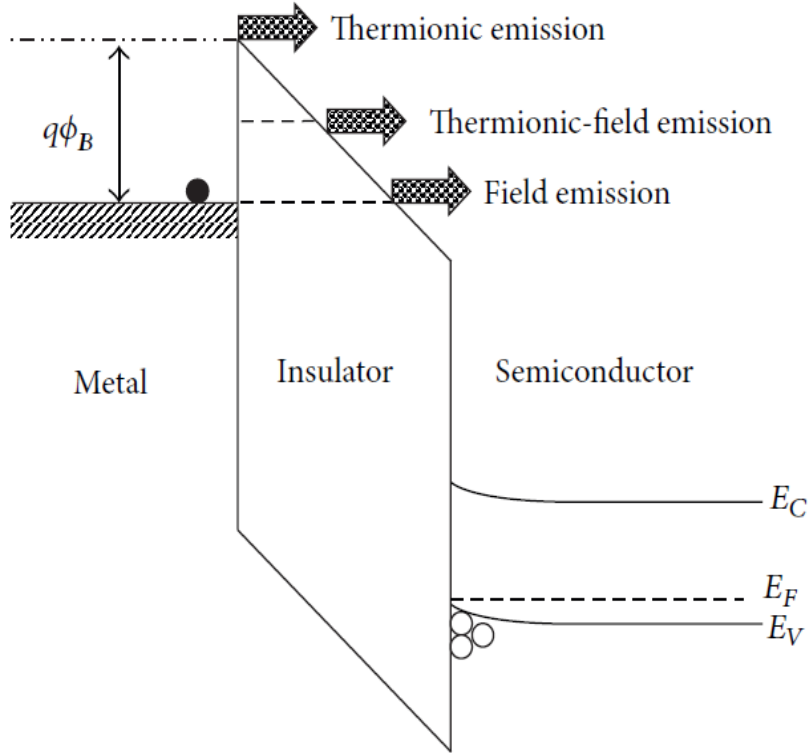
Figure 11. Thermionic-field emission mechanism.

1.3.2 Bulk-limited conduction

While in bulk-limited current injection, the behaviour of carriers is governed by the dielectric properties such as defect density, permittivity, and electron mobility.

a). Poole-Frenkel (P-F) emission

P-F emission occurs when the electrons are pumped from traps to the conduction band by thermal excitation. The applied voltage could reduce the potential

barrier which traps the electron, therefore thermal excitation will be more likely to help electrons get out of the trap. Figure 12 shows the mechanism of P-F emission in an MIS structure.
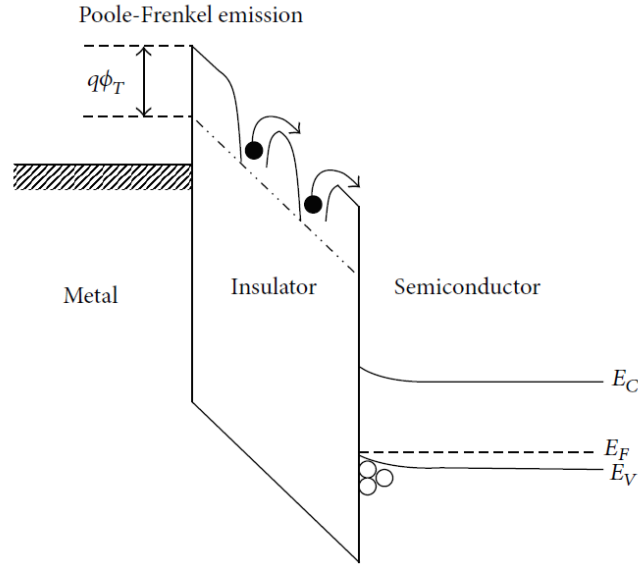
Figure 12. Poole-Frenkel emission in MIS structure.

The current density can be defined as:

$$J = q\mu N_c E \exp\left[\frac{-q\left(\phi_T - \sqrt{qE/\pi\varepsilon_i\varepsilon_0}\right)}{kT}\right] \qquad (1.6)$$

Where μ is the carrier mobility, N_c is the density of states (DOS) in the conduction band, and $q\phi_T$ is the potential barrier of the trap. The plot of $\log(J/E)$ versus $E^{1/2}$ should be a linear curve.

b). Hopping conduction

Hopping conduction is the process in which the carriers hop from one trap site to another trap site due to tunneling effects and then travel through the dielectric film. Figure 13 shows the process of hopping conduction in an MIS structure.
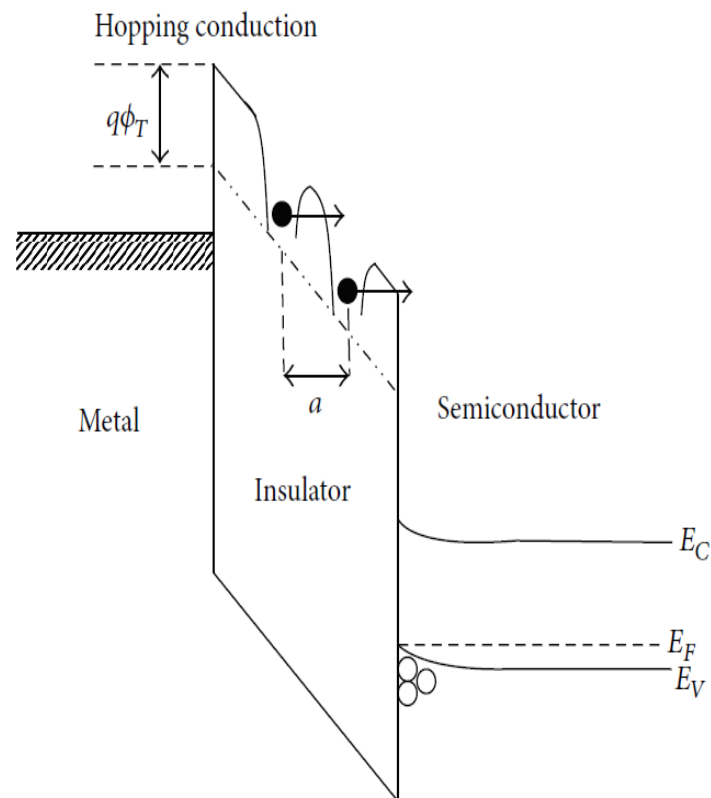
Figure 13. Hopping conduction in MIS structure.

The current density in hopping conduction is:

$$J = qanv \exp\left[\frac{qaE}{kT} - \frac{E_a}{kT}\right] \qquad (1.7)$$

Where a is the mean hopping distance or the distance between trap sites, n is the carrier concentration in the conduction band, v is the frequency of the thermal vibration of electrons at trap sites, and E_a is the energy gap between the trap state to the conduction band.

c). Ohmic conduction

Ohmic conduction occurs for the electrons in the conduction band and the holes in the valance band. The current density versus the electric field should be a linear curve.
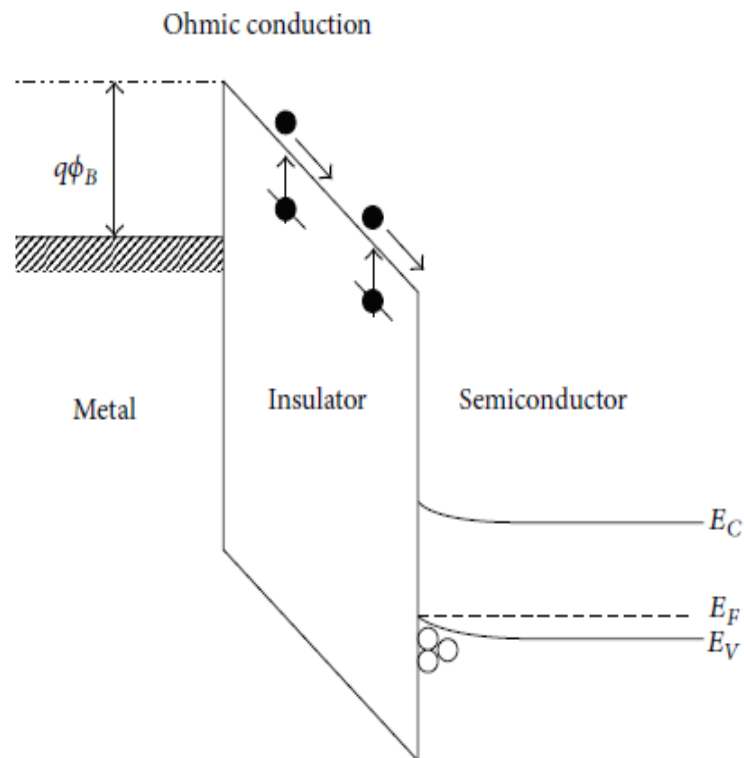
Figure 14. Ohmic conduction in MIS structure.

There will be a small number of carries generated contributing to Ohmic Conduction, despite the large band gap of the dielectric layer. However, this conduction mechanism can be negligible when the temperature is low due to the lower possibility of thermal excitation.

1.4 Thesis goal and outline

The objective of this thesis project was to investigate the optical and electrical properties of silicon-based light emitting devices with Ce doping, for integrated photonics and solid-state lighting applications.

The samples were deposited using electron-cyclotron-resonance plasma enhanced chemical-vapor deposition (ECR-PECVD) with in-situ Ce^{3+} doping on silicon substrates. Oxygen was gradually substituted by nitrogen to produce SiO_xN_y thin films with different layer compositions. Refractive indices extracted from variable-angle spectroscopic ellipsometry (VASE) measurements classified the thin films into two main groups, SiO_x and SiO_xN_y. The thin film composition was studied by Rutherford Backscattering Spectrometry (RBS), verifying the gradual increase in nitrogen content. Photoluminescence (PL) spectra of samples were obtained using a 375 nm laser diode as an excitation source and quantum efficiencies (QE) of all samples are calculated. All samples were subjected to the post-deposition annealing treatment for 1 hour at different temperatures varying from 800 to 1200°C in both 95% N_2 and 5% H_2 and pure N_2 gas environment, to investigate the effect of hydrogen passivation on the PL irradiance. Samples subjected to annealing

yield considerably stronger blue/white PL emission than as-deposited ones, due to the formation of Ce-containing clusters at an annealing temperature of 900 °C. The optimum layer composition and annealing condition to produce SiO_xN_y thin films with maximized Ce^{3+} excitation efficiency was determined. Besides, the effect of hydrogen fluoride (HF) etching on PL irradiance was studied, showing that an HF (1%) etching duration of 90 s yields the highest PL irradiance. Finally, the samples were coated with indium tin oxide (ITO) and aluminum on the front and backside respectively, as preliminary work for electrical characterization. I-V measurements were conducted for all samples, showing a good carrier injection ability.

2. Fabrication Methodologies

2.1 Introduction to the ECR-PECVD system

Samples were deposited using an electron cyclotron resonance plasma enhanced chemical vapor deposition (ECR-PECVD) system. A schematic illustration of the ECR-PECVD system is shown in Figure 16. A load-lock (LL) chamber is used to isolate the deposition (main) chamber from the atmosphere. As the sample has been loaded on the vertical arm in the LL chamber and the pressure in LL chamber drops below 10^{-7} mTorr, the sample will be transferred to the deposition chamber through the gate between load-lock and the main chamber. The sample will then be transferred from the vertical arm to the rotating stage. Before deposition, the main chamber will be pumped to an ultra-high vacuum of $10^{-8} – 10^{-9}$ mTorr, where the real-time pressure will be monitored by a hot cathode ion gauge. Before the actual deposition starts, an Ar plasma cleaning needs to be performed to remove the organic residuals on the wafer surface. Next, the sample stage will rotate at a speed of 25 rpm and be heated up to 135 °C. During the deposition, 30% SiH_4 in Ar, 10% N_2 in Ar, 10% O_2 in Ar, and pure N_2 were used as precursor gases for a 60-min deposition on 3" Si (100) substrates. The microwave source is used to enable the resonance with electrons to ionize the precursor gases with a power of 500 W and a frequency of 2.45 GHz[29]. Figure 15 shows the plasma generated in the deposition chamber of ECR-PECVD system. A detailed discussion of the ignition of an ECR plasma

can be found in a former group member's Master's thesis[30]. And finally, the in-situ doping of Ce is performed by running Ar gas through a heated (215 °C) metal cell which contains volatile Ce metal-organic powder (Ce[tmhd]4) from Strem Chemicals Inc.
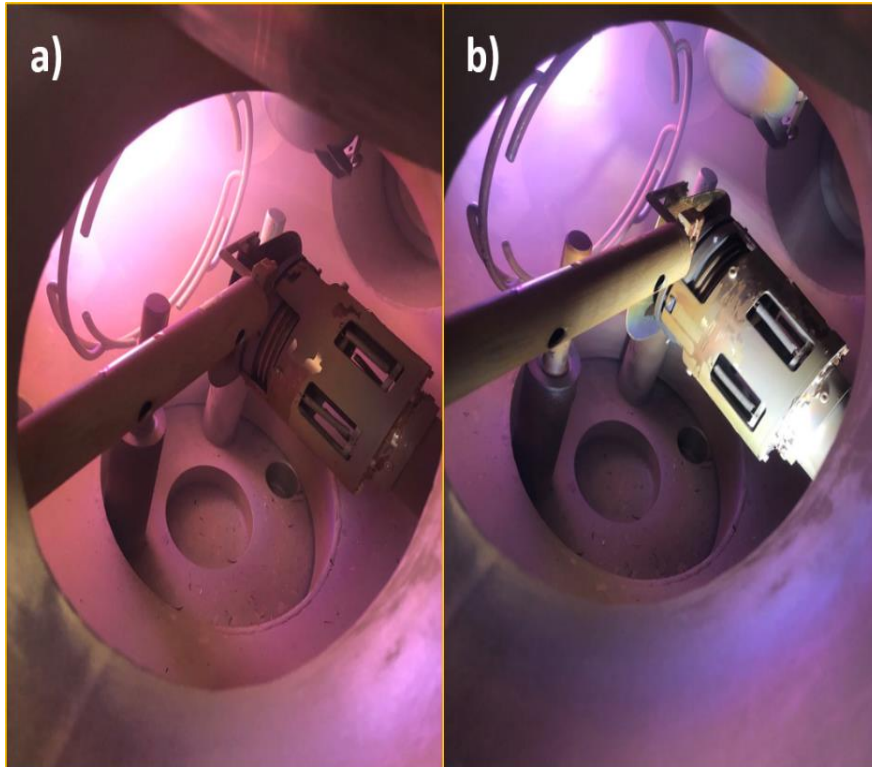
Figure 15. Plasma ignition in the deposition chamber with different precursor gases: a). majority of the gas being nitrogen; b). majority of the gas being oxygen.

The ECR-PECVD system has several advantages over a conventional PECVD system. In the conventional PECVD system, ionized particles with high energy are likely to damage the substrate and the thin film, as well as to deposit undesired materials[25]. In the ECR-PECVD system, this issue should not be a

concern since the substrate and thin film are at a distance from the remotely generated plasma. Most importantly, the ECR-PECVD system is capable of doing in-situ rare-earth doping during the thin film deposition without compromising the thin film quality. This kind of doping can yield better uniformity and larger RE incorporation than that of conventional doping methods[31]. More details about the system can be found in the former researchers' work in the group[32,33].
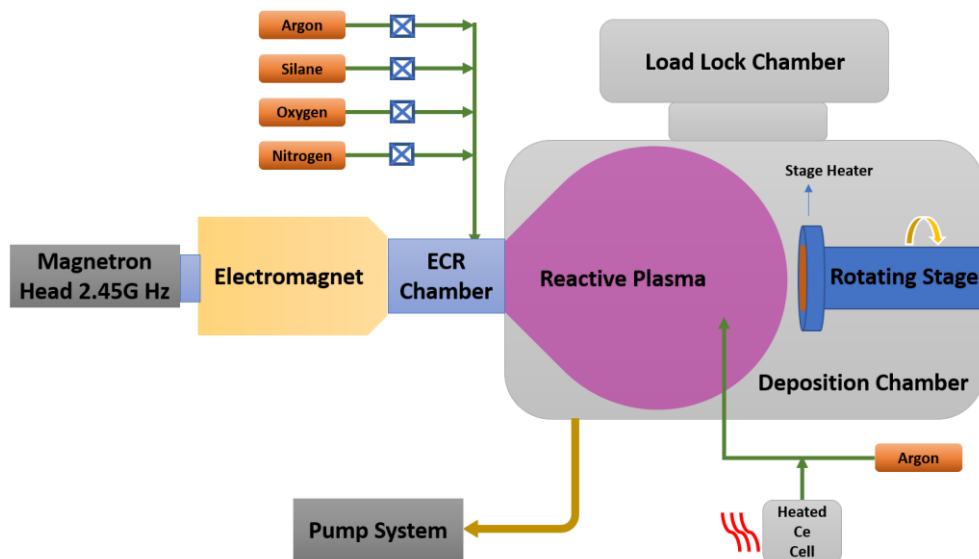
Figure 16. A schematic illustration of the ECR-PECVD system.

2.2 Sample depositions

A set of six Ce-doped samples was deposited with the same Ce concentration (same Ce cell temperature and Ar flow rate) but different host materials (SiO_x,

SiO_xN_y, and SiN_x). A gradual change in the precursor gases from O_2 to N_2 was performed during the deposition, to investigate the role of nitrogen on the photoluminescence properties.

Table 1. Gas flow rates and partial gas pressures of precursor gases.

Samples	SiH_4/Ar (sccm/m Torr)	N_2/Ar (sccm/m Torr)	O_2/Ar (sccm/m Torr)	Ar (sccm/m Torr)	Ce/Ar (sccm/m Torr)
SiO-0	2/0.30	0/0	28/3.00	10/0.85	0/0
SiON-7	2/0.30	7/0.95	21/2.25	10/0.95	0/0
SiON-14	2/0.30	14/1.5	14/1.75	10/0.95	0/0
SiON-21	2/0.30	21/2.25	7/1.00	10/1.00	0/0
SiN-28	2/0.30	28/3.00	0/0	10/1.00	0/0
CeSiO-0	2/0.25	0/0	28/2.90	0/0	10/0.85
CeSiON-7	2/0.25	7/0.85	21/2.20	0/0	10/0.90
CeSiON-14	2/0.25	14/1.40	14/1.45	0/0	10/0.90
CeSiON-21	2/0.25	21/2.20	7/1.00	0/0	10/0.90
CeSiN-28	2/0.25	28/2.80	0/0	0/0	10/0.95
CeSiN-Pure	2/0.25	28/2.60	0/0	0/0	10/0.90
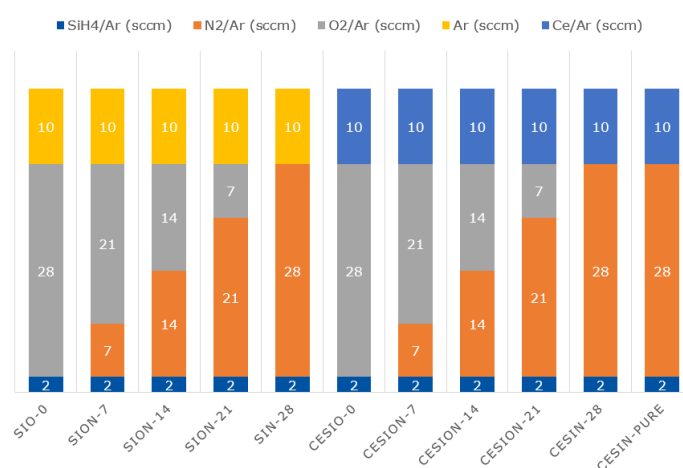
Figure 17. Column chart of deposition parameters.

The second batch of reference samples was also fabricated with the same deposition parameters but without any Ce-doping. The details of the deposition parameters can be found in Table 1 and Figure 17. Samples are noted by the deposition recipe and the number in the sample labels the nitrogen flow rate (sccm). For instance, a sample with Ce doping deposited with saline, oxygen, and 7 sccm diluted nitrogen is denoted as CeSiON-7. The oxygen flow rate is compensated to keep the total flow rate and main chamber pressure constant at 40 sccm and 4.0 mTorr, respectively.

2.3 Post-deposition annealing (PDA)

Figure 18. Quartz tube furnace for post-deposition annealing.

As-deposited (AD) Ce-doped and reference samples were subjected to post-deposition annealing at temperatures ranging from 800 to 1200 °C for 1 hour in a quartz tube furnace. N_2 and a mixture of 95 % N_2 and 5 % H_2 (NH) were used,

respectively for the annealing to study the effect of hydrogen passivation on the photoluminescence properties and the effect of PDA on charge carrier injections.

The quartz tube furnace consists of a 3-zone furnace from Lindberg Hevi-Duty company and a 3-zone PID controller from Eurotherm. A quartz boat with a quartz rod was used for loading and unloading samples. To perform annealing, the temperature in the furnace should be controlled to ramp up slowly. To perform annealing at 1200 °C, the temperature firstly should be set to 500 °C then raised to 900 °C after 1 hour to make the temperature stable. Then the temperature could be raised to 1200 °C after it stays at 900 °C for another hour. During ramping up, Ar should be used to purge the quartz tube in order to create a noble gas environment for annealing as well as to prevent oxygen contamination from the outside atmosphere. It is worth mentioning that the samples are at high temperature after 1200 °C annealing, so it would attract oxygen contamination if exposed to air. A good way to avoid this situation is to turn off the furnace and leave the samples in the furnace overnight with continuous noble gas purging.

2.4 ITO and Al coating

Radio frequency (RF) magnetron sputtering was used to coat the samples with ITO and aluminum as electrodes for electrical characterization. Compared to the direct current (DC) sputtering technique, which is limited when it comes to

dielectric non-conducting or insulating target materials, RF sputtering can coat these materials on the substrate with good uniformity[34]. Figure 19 (a) shows the working principle of a RF magnetron sputtering system. Inert gases in the vacuum chamber will be ionized by the energetic wave from the RF system. The target material is bombarded by the high energy ions and then moves to the substrate to be coated.
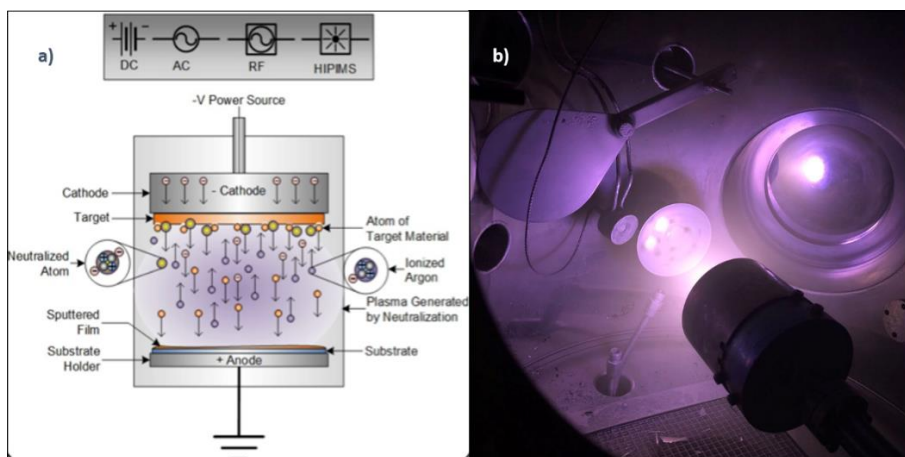
Figure 19. a). Schematic illustration of an RF sputtering system; b) Sputtering image taken by a cell phone camera with 10 Mega pixel[34].
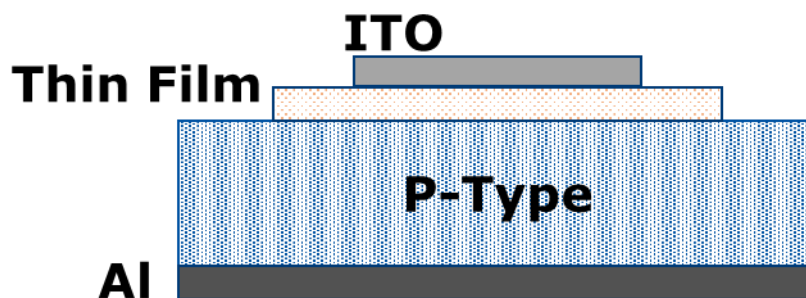
Figure 20. Cross section of sample structure after magnetron sputtering.

In order to control the pattern of the ITO electrode on the top surface of the samples, the samples are covered with a shadow mask. The samples will be coated with the ITO electrode on the parts where the metallic mask is not covering the samples, so the desired electrode shape could be patterned. The samples are then mounted on the sample holder, which will be rotating at a speed of 100 rpm corresponding to a motor voltage of 20 V. After loading the samples into the chamber, the chamber will be pumped down to high vacuum at 10^{-7} mTorr during a period of 2 hours. For ITO coating, 36 sccm Ar and 0.2 sccm O_2 are introduced to the chamber to reach a pressure of 20 mTorr in order to initiate the plasma. The role of O_2 here is to increase the transparency and the conductivity of the coated ITO. The sputtering duration for ITO is 49 minutes and it yields an ITO thickness of 200 nm. For aluminum coating, only 10 sccm Ar is needed, and a duration of 20 minutes would yield a thickness of 200 nm. Figure 20 shows the Cross section of sample structure after magnetron sputtering.

2.5 Rapid thermal annealing (RTA)

Annealing treatment of the as-deposited ITO coating can improve the layer crystallinity and eliminate the defect sites in the coating[25]. This process is called rapid thermal annealing (RTA). The defect sites could reduce the conductivity and transparency due to their ability to trap injected carriers and incident photons. The JETFIRST 150 system from JIPELEC Inc. with capability of 4"

or 6" wafer processing was used for the purpose of RTA. To perform RTA, the samples have to be loaded in the carbon sample holder. The software JETFIRST will be used to load the RTA recipe and control the RTA process. The temperature, measured by a K type (Chromel/Alumel) thermocouple with a diameter of 0.127 mm, will ramp up fast to 400 °C with a rate of 25 °C/s under flowing N_2 gas and keep annealing for 1 minute.
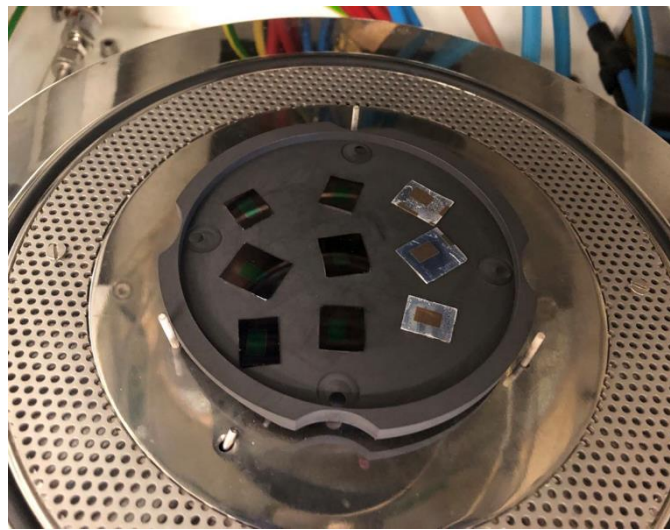
Figure 21. Sample holder for RTA.

3. Sample Characterization Methods

3.1 Rutherford Backscattering Spectrometry

Rutherford Backscattering Spectrometry (RBS) is a non-destructive technique to analyze the composition of a material quantitatively. Besides, it has a good resolution and sensitivity to heavy elements[25]. Figure 22[35] shows the typical setup of a simplified RBS diagram. A highly energetic charged He ion beam is incident on the sample. Part of the incident ions will be backscattered to a solid-state nuclear particle detector due to the elastic collision.
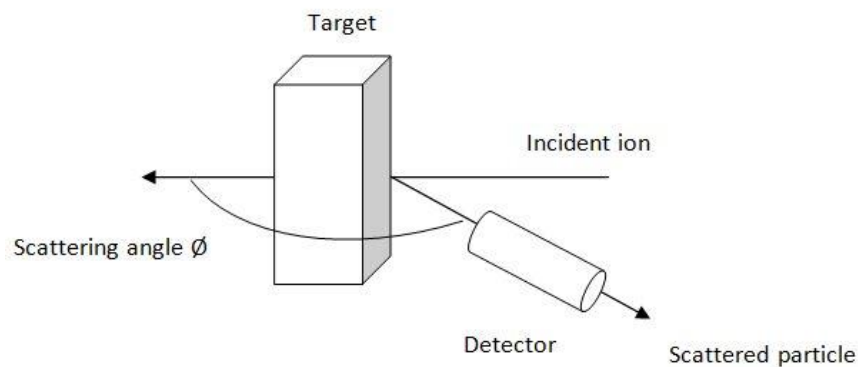
Figure 22. Illustration of RBS setup[35].

The kinematics of two particles in an elastic collision can be solved by using the law of conservation of energy and momentum.

The ratio between the energy of the incident ion (E_{in}) and the target atom (E_{ref}) after the collision can be obtained as:

$$\frac{E_{ref}}{E_{in}} = \left[\frac{\left(M_2^2 - M_1^2 \sin^2 \theta\right)^{\frac{1}{2}} + M_1 \cos \theta}{M_1 + M_2}\right]^2 \qquad (3.1)$$

Where M_2 and M_1 are the masses of the incident and the targeted nuclei respectively and θ is the scattering angle. This ration is defined as the kinematic factor K. The energy gain ration (E_{tar}) of the target atom can be easily obtained:

$$\frac{E_{tar}}{E_{in}} = 1 - \frac{E_{ref}}{E_{in}} \qquad (3.2)$$

Energy loss in this process is always below 100 keV and can be considered negligible compared to the high energy flux in the range of MeV. The depth profile of the element of interest can be obtained in an RBS spectrum, due to the energy loss of incident ions when penetrating the target. An in-depth review of the RBS technique can be found in M. Mayer's publication[36].

The RBS facility is located in the Tandetron Accelerator Laboratory at Western University in London, Ontario, Canada. Samples are measured by using a Cornell geometry, where the samples rotate, and the incident and reflected beams are on one plane, making the measurement more accurate. Figure 23 shows the mounted samples for RBS measurement. The detector angle was fixed at 170 degrees. ^{4}He$^+$ with a dose of 3 μC with an energy of 1.8 MeV for Ce samples (2.4 MeV for reference samples) were used. A standard reference sample (SiSb$_3$) with an antimony concentration of $4.67 \times 10^{15}/cm^2$, was used for the calibration. The RBS spectra were analyzed using the SMNRA

software[37] and the stopping power is obtained from Ziegler data[38].

Figure 23. Sample mounted for RBS measurements.

Figure 24 shows a typical RBS spectrum and simulation of the CeSiO-0 sample. The corresponding peaks of Si, O, and Ce are marked in the figure. Heavier atoms - such as Ce - will sit on the high energy side on the x-axis, due to a larger kinematic factor K. A good simulation was obtained for sample CeSiO-0. Broad peaks of different elements indicate uniform doping through the entire thin film. An atomic concentration of 1.49×10^{17} at/cm^2 was calculated for Si, 3.31×10^{17} at/cm^2 for O, 4.99×10^{15} at/cm^2 for Ce, corresponding to 25.6%, 57.3%, and 0.9% in the thin film composition, respectively. The residual composition of the sample is considered to be and simulated as hydrogen since

hydrogen cannot be determined using the RBS technique.
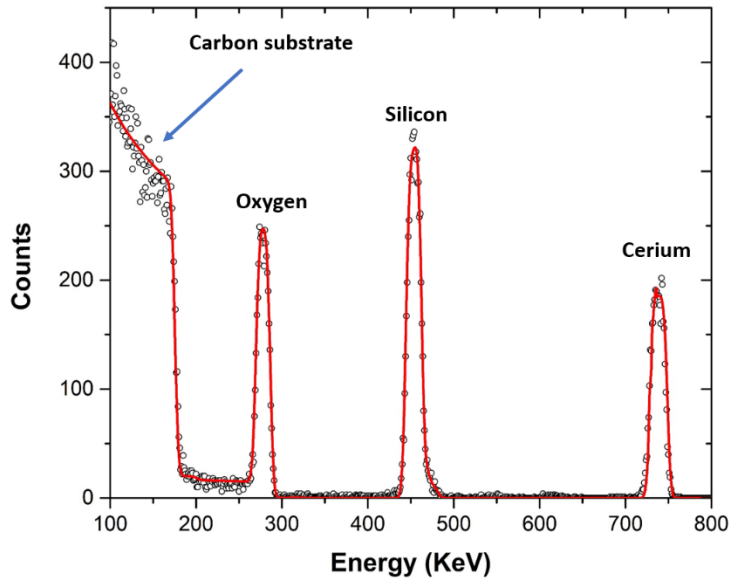
Figure 24. RBS spectrum of sample CeSiO-0 with simulated data (red line). Each peak represents a different element.

1 mm thick carbon substrates are used during the ECR-PECVD depositions for RBS measurement purposes. A carbon atom is lighter than all the elements in the samples so it would appear on the left side of the RBS spectrum without overlapping the signal from other elements, making the measurement and simulation more precise.

3.2 Variable Angle Spectroscopic Ellipsometry

Variable Angle Spectroscopic Ellipsometry (VASE) can be used to determine the optical properties and the film thickness of all the thin film samples. Figure

25 shows the experimental setup of a J.A.Woollam M-2000U UV-Vis ellipsometer with near-infrared extension (246 nm to 1688 nm). A polarized light beam is incident on the sample and then is reflected and collected by a detector. The optical properties of the sample measured can be obtained from the information of the polarization change of the collected beam.

Figure 25. VASE system setup[39].

The mathematical theory for VASE analysis is based on the Fresnel reflection/transmission equations by solving Maxwell's equations. The change of Psi (Ψ) and the phase difference between incident and reflected light Delta (Δ) are usually of interest in a VASE measurement:

$$\tan(\Psi)e^{i\Delta} = \rho = \frac{r_p}{r_s} \qquad (3.3)$$

Where r_p and r_s are the complex Fresnel reflection coefficients of the sample for polarized light in the incident plane and perpendicular to the incident plane, respectively.
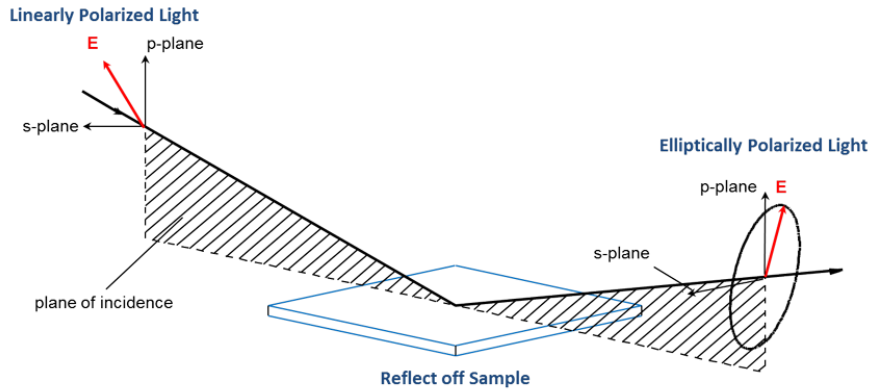
Figure 26. Schematic of a VASE measurement[39].

The VASE data is the spectrum of Ψ and Δ as a function of both wavelength and angle of incidence. The Cauchy model can be used to model the VASE data and the three-term form of Cauchy's equation is:

$$n(\lambda) = A_n + \frac{B_n}{\lambda^2} + \frac{C_n}{\lambda^4} \qquad (3.4)$$

Where n is the refractive index, λ is the wavelength, A_n, B_n, C_n are the coefficients that can be determined by substituting the refractive indices at known wavelengths into equation (3.4)[40]. The Cauchy model is based on the assumption that the thin film is fully transparent (non-absorbing) to the light of

all wavelengths which is not realistic. However, for VASE measurements using short wavelength light (UV range), the model can yield more reliable results of sample thickness and refractive index. Measurements using 5 different incident angles (55°, 60°, 65°, 70° and 75°) can further improve the accuracy.

The simulation and fitting process is conducted using J.A.Woollam's CompleteEASE software package[41]. In most cases, as-deposited samples should be used for VASE measurement. Nanostructures formed in annealed samples would require more advanced analysis and bring uncertainties to the VASE measurement. Therefore, AD samples provide the most accurate and consistent information of the samples when one makes comparison between different samples. In general, fits with a mean squared error (MSE) lower than 20 would be considered acceptable.

3.3 Photoluminescence

The light emission characterization of Ce doped samples was performed using the PL technique. As shown in figure 27, when the sample absorbs a photon with energy higher than the bandgap of the materials itself, the electron in the valance band of the sample will be excited to the conduction band. Then the electron may drop back to the valence band through so-called radiative recombination, during which a photon with the energy of the material bandgap will be emitted. This process is called photoluminescence.
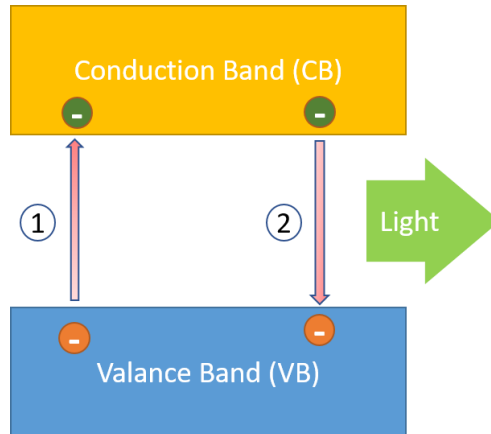
Figure 27. Simple illustration of the PL process.

Figure 28 shows the room temperature PL setup used for this thesis. A 375 nm laser beam from a laser diode (Coherent OBIS 375) was directed on to a sample mounted on the sample holder, via a mirror that can reflect light in the UV range with negligible loss. The power of the laser is controlled using a Coherent OBIS Laser Controller and Coherent Connection software package. The power of the laser was set at 45 mW (90% of the maximum power) for all PL measurements. A 400nm long-pass filter is placed in front of the detector to prevent the high-power laser from saturating the detector. The light emission from the sample was collected by an Ocean Optics USB2000+ CCD/Spectrometer and the signal is transmitted to a computer via A/D converter. The data was processed in the software OOIIrrad from Ocean Optics, Inc[42]. To process the PL spectrum, we used an integrating time of 5000 ms, an average of 5 scans, and a smoothing size of 5 points, which averages 5 adjacent data points on the spectrum. The dark spectrum will be subtracted from the PL

spectrum which needs to be taken before the measurement starts. The response of the system will be applied to the PL data for correction. The system response used was obtained by a former group member, O. Zalloum[43].
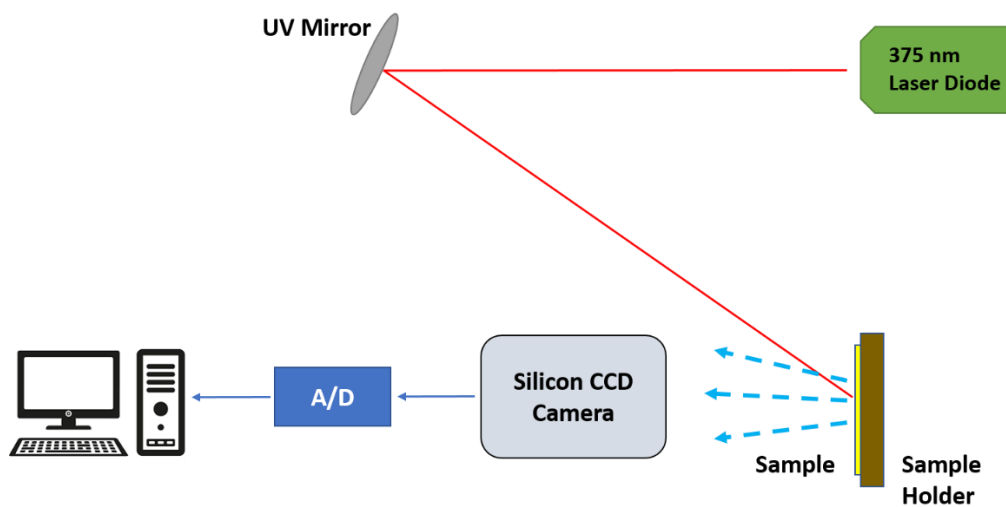
Figure 28. Schematic of room temperature PL setup.

3.4 I-V measurements

The goal of an IV measurement is to explore the behavior of charge carriers and characterize the conduction mechanism in dielectric thin films.

To obtain the I-V curve, an Agilent 6624A SYSTEM DC POWER SUPPLY is used to provide electric power to the measurement circuit. A KEITHLEY 6485 PICOAMMETER is used to measure the current flow. Figure 29 shows the metal tips of the cathode and anode for I-V measurement. The

two instruments were programmed using LabVIEW where the program was developed by former group member B. Lee.
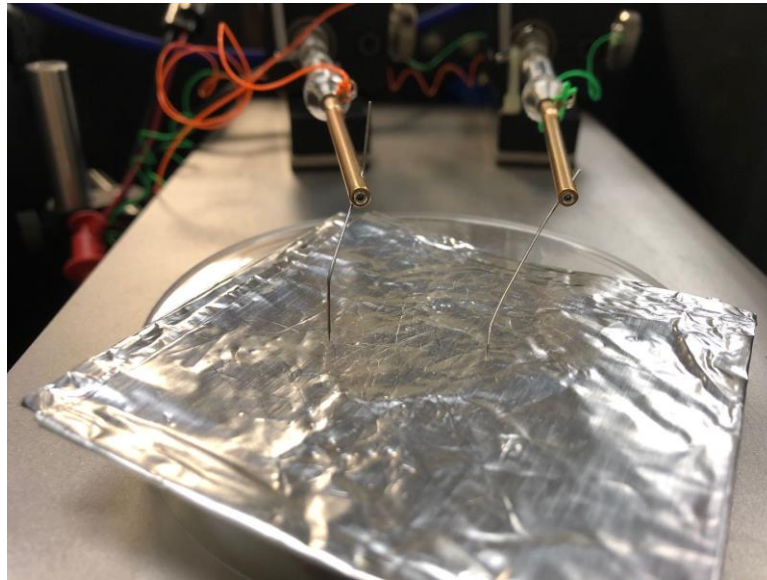
Figure 29. Metal tips of cathode and anode for I-V measurement.

4. Study of Ce-doped Samples

4.1 Elemental compositional analysis

Elemental compositional analysis was carried out for all Ce-doped samples and reference samples without any Ce doping. All samples will be discussed in detail in this section.
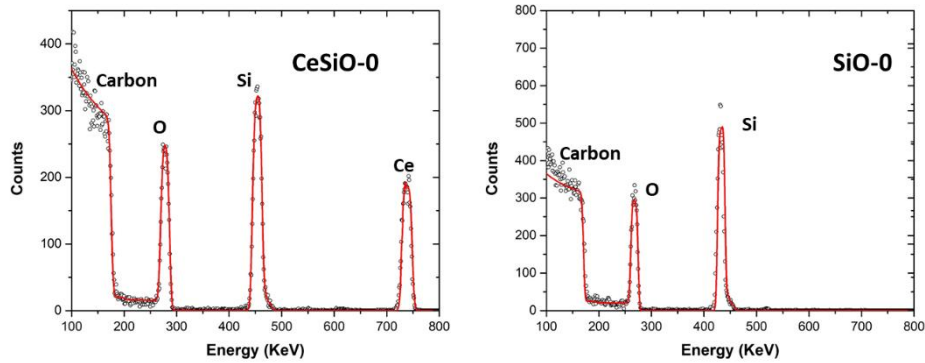
Figure 30. RBS spectra of CeSiO-0 and SiO-0.

The RBS spectrum of AD CeSiO-0 and AD reference sample SiO-0 are shown in figure 30. The black dots are the experimental data and the red line is the simulation. Good fitting was obtained for the spectra. In the CeSiO-0 sample, the concentrations of Si, O, and Ce are 25.6%, 57.4%, and 0.9% (significant figures maximum 3, correct for the following data), respectively. In the SiO-0 sample, the concentrations of Si and O are 35.4% and 65.6%, respectively. Although the SiO-0 sample is the reference sample of CeSiO-0 for the purpose

of investigating the role of Ce dopants, the concentration of Si in SiO-0 is around 10% higher than the Si content in CeSiO-0, and the concentration of O in SiO-0 is around 8% higher than O in CeSiO-0. This phenomenon is also observed in other Ce-doped and reference samples. The only difference during the deposition process of these two samples is the introduction of the Ce metal-organic precursor. The undesired contamination in the CeSiO-0 sample is likely to originate from the Ce metal-organic gas. Besides, the difference in the plasma due to different precursor gases would also contribute to the thin film growth, resulting in different thin film composition.

Figure 31. PBS spectra of CeSiON-7 and SiON-7

Figure 31 shows the RBS spectra of AD CeSiON-7 and AD reference sample SiON-7. In the CeSiON-7 sample, the concentrations of Si, O, N and Ce are 26.5%, 57.1%, 0.9%, and 0.6%, respectively. In the SiON-7 sample, the concentrations of Si, O, and N are 34.5%, 64.7%, and 0.9%, respectively. N can

be observed from the RBS spectrum from this point during the gradual substitution of O2 with N2. However, the concentration of N is very low.

Figure 32 shows the RBS spectra of AD CeSiON-14 and AD reference sample SiON-14. In sample CeSiON-14, the concentrations of Si, O, N and Ce are 26.5%, 57.1%, 0.9%, and 0.6% respectively. In SiON-14 sample, the concentration of Si, O, and N are 34.5%, 64.7%, and 0.9%, respectively. However, the peak of N is not visible on the RBS spectrum due to its low concentration. The concentration of N was obtained from the fitting function of SIMNRA software.
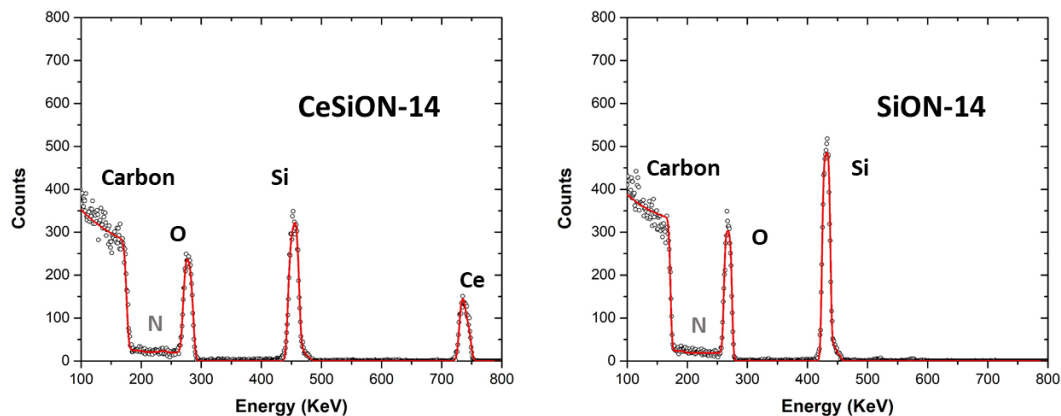
Figure 32. RBS spectrums of CeSiON-14 and SiON-14.

Figure 33 shows the RBS spectrum of AD CeSiON-21 and AD reference sample SiON-21. In sample CeSiON-21, the concentrations of Si, O, N and Ce are 26.0%, 53.6%, 4.6%, and 0.6%, respectively. In the SiON-21 sample, the concentrations of Si, O, and N are 36.1%, 56.2%, and 7.7%, respectively.

Compared to CeSiON-14 and SiON-14, the N peak started to emerge in the RBS spectrum due to the increase of nitrogen flow during the deposition.
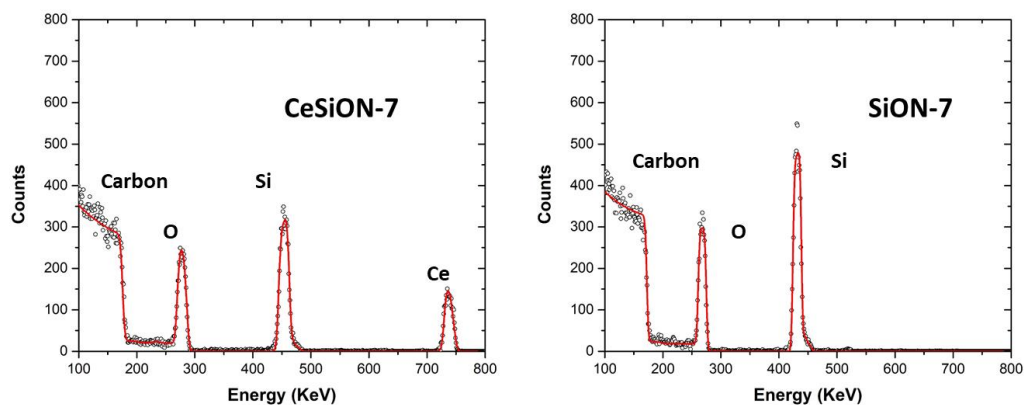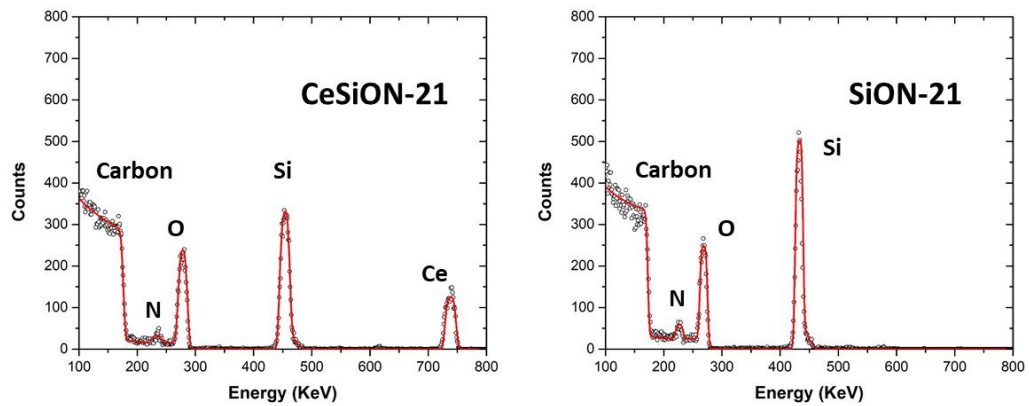

Figure 33. RBS spectra of CeSiON-21 and SiON-21.

Figure 34 shows the RBS spectra of AD CeSiN-28 and AD reference sample SiN-28. In sample CeSiN-28, the concentrations of Si, O, N and Ce are 24.5%, 55.4%, 5.3%, and 0.8%, respectively. In the SiN-28 sample, the concentrations of Si, O, and N are 35.6%, 44.7%, and 19.7%, respectively. Instead of using both oxygen and nitrogen as ECR-PECVD precursors, no oxygen was introduced in the deposition chamber during the thin film growth. However, undesired oxygen contaminations in both CeSiN-28 and SiN-28 samples were observed in the RBS spectrum. This undesired oxygen contamination was also observed in the SiN_x deposited previously by the same ECR-PECVD system[44]. It is suggested that part of the undesired oxygen originates from the volatilized metal-organic gas (Ce[tmhd]$_4$) that contains

oxygen in its molecular formula ($C_{44}H_{76}CeO_8$). Other sources of oxygen contamination might be the impurity of the precursor gases and a potential leak of the ECR-PECVD system. Besides, the N concentration in sample SiN-28 (19.7%) is much higher than it in CeSiN-28 (5.3%), which is likely to result from the different thin film growth due to different precursor gases used.
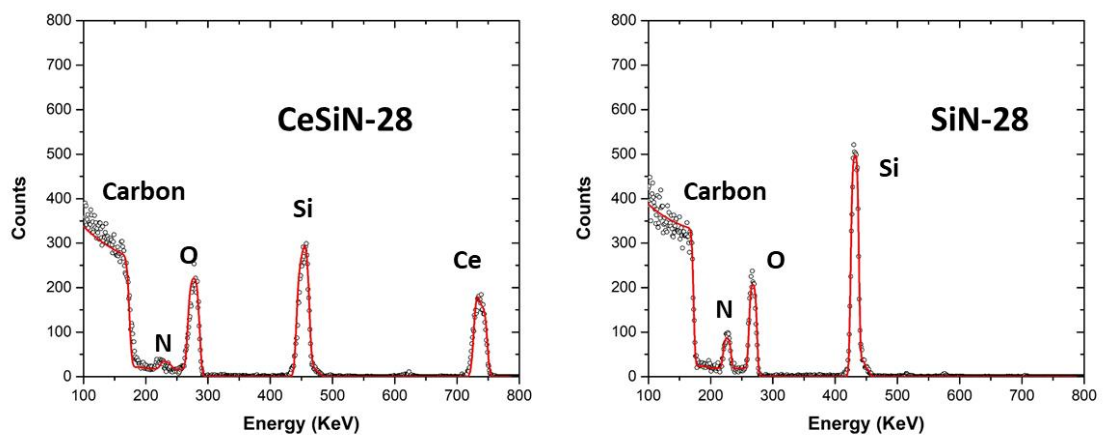
Figure 34. RBS spectra of CeSiN-28 and SiN-28.
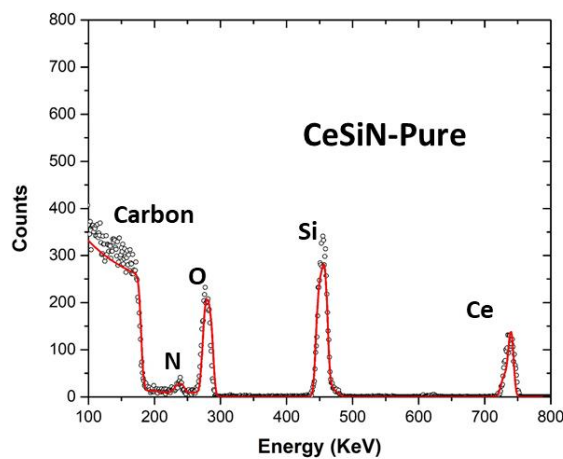
Figure 35. RBS spectrum of CeSiN-pure.

Lastly, the RBS spectra of AD CeSiN-pure is shown in figure 35. In sample CeSiN-pure, the concentrations of Si, O, N and Ce are 22.3%, 48.6%, 5.2%, and 0.5%, respectively. Compared to CeSiN-28, pure nitrogen gas instead of diluted nitrogen in argon was used to deposit SiN_x thin films. A large portion of oxygen present in the RBS spectrum confirmed that the diluted nitrogen does not contribute to the oxygen contamination. Besides, the atomic content for all other elements remained at the same level as in samples deposited using diluted nitrogen.
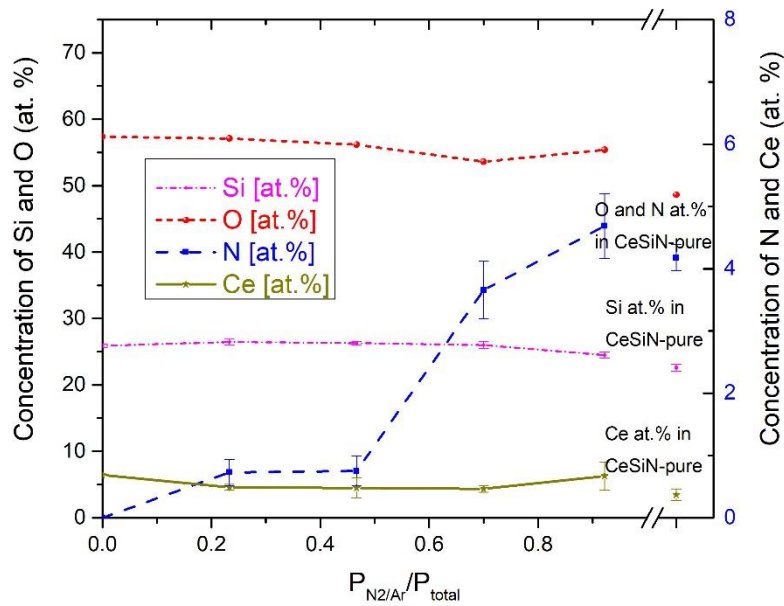
Figure 36. Concentrations (at. %) of Si, O, N, and Ce in Ce-doped samples as a function of the relative N₂/Ar flowrate (sccm) during deposition.

Figure 36 shows the elemental composition versus the relative partial pressure of 30% N2: Ar and the total pressure in the deposition chamber during

the sample fabrication, of the Ce-doped SiOx, SiOxNy, and SiNx samples. The concentrations of Si (purple) and O (red) correspond to the left axis, and the concentrations of N (blue) and Ce (brown) correspond to the right axis. Concentrations of different elements in CeSiN-pure are also marked on the figure.

Good fits were obtained for all RBS spectra. The concentrations of Si, O, and Ce fluctuated slightly across all samples (Si at. 22.3 % – 26.5 %, O at 48.6 – 57.4 %, Ce 0.5 – 0.9 %). With the increase in the N_2:Ar precursor gas flow during the deposition, a gradual increase of N concentration is observed from 0 % to 5.2 %. This could also be used as the calibration data for the ECR-PECVD system to grow silicon nitride thin films.

4.2 Variable Angle Spectroscopic Ellipsometry

The thicknesses and refractive indexes were obtained from VASE measurements for all Ce doped samples and reference samples.

Figure 37 shows the change of sample thicknesses and refractive indexes, as a function of the ratio between the partial pressure of 30% N_2: Ar and the total pressure in the chamber during sample fabrication, in all reference samples. The red dots correspond to the film thickness and blue dots correspond to the refractive index at a wavelength of 632.8 nm. The thicknesses of the samples are nearly constant at around 900 Å. The refractive index evolved from 1.45 to

1.67, reflecting that Si_3N_4 has a higher refractive index of 2.3 than stoichiometric SiO_2 (1.45)[45].
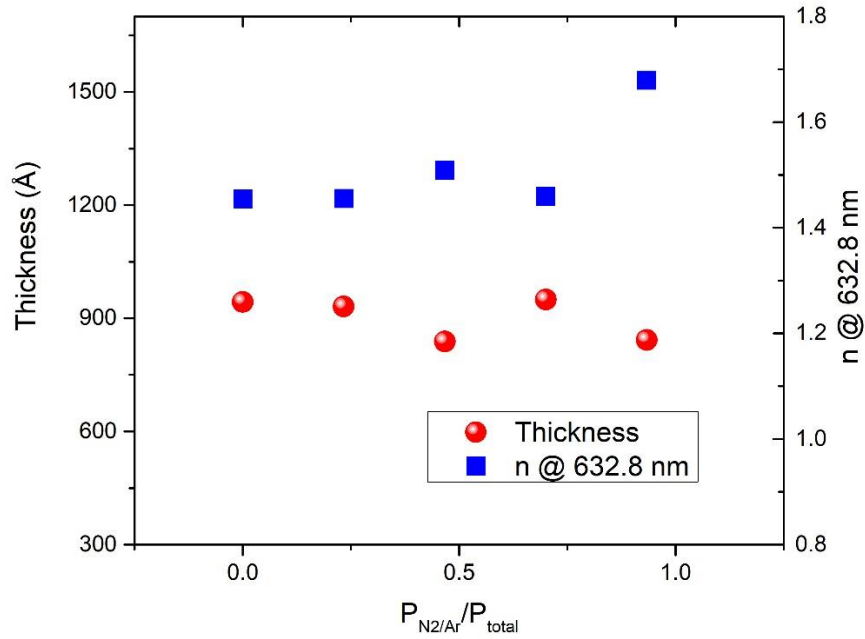
Figure 37. The thicknesses and refractive indexes of reference samples as a function of partial pressure of nitrogen during deposition.

Table 2. VASE fitting parameters for reference samples.

Samples	MSE	A	B	C
SiO-0	3.405	1.454	0.00393	0.00003
SiON-7	4.527	1.455	0.00341	0.00007
SiON-14	4.101	1.509	0.00292	0.00017
SiON-21	4.879	1.459	0.00306	0.00010
SiN-28	4.241	1.679	0.00825	0.00015
Average	4.23071	1.51116	0.00432	0.00011
Std.Dev.	0.54942	0.09649	0.00224	0.00006

For the batch of reference samples, an average MSE of 4.23 was obtained, indicating a good match between the experimental data and the fits. The fitting parameters including MSE and the Cauchy coefficients A, B, and C for equation (3.4) can be found in Table 2.
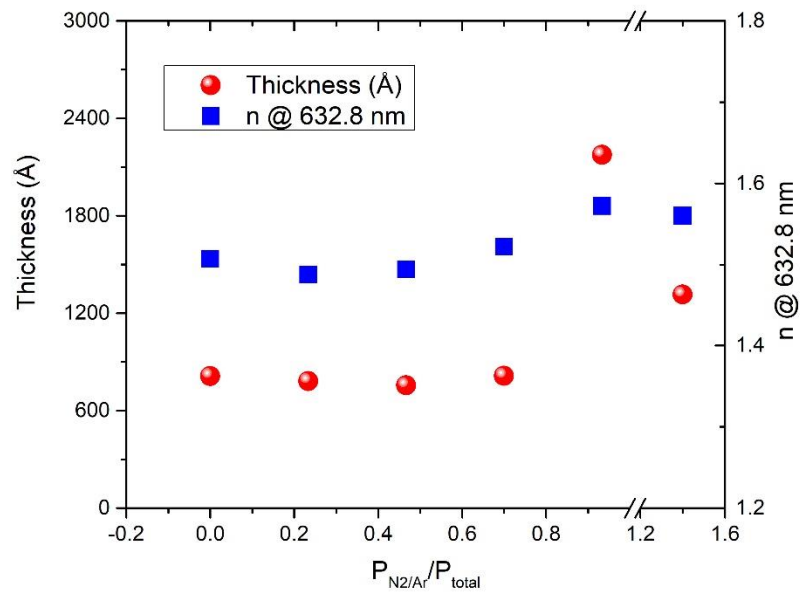
Figure 38. The thicknesses and refractive indexes of Ce-doped samples as a function of the partial pressure of nitrogen during deposition.

Figure 38 shows the change of sample thicknesses and refractive indexes, as a function of the ratio between the partial pressure of 30% N_2: Ar and the total pressure in the chamber during sample fabrication, in all Ce-doped samples. The thicknesses of the samples are constant at around 850 Å expect for samples CeSiN-Pure and CeSiN-28, which yield thicknesses of 1376 Å and 2168 Å, respectively. The refractive index evolved from 1.48 to 1.55 due to the

stoichiometric changes of the thin films. The thickness of the CeSiN-28 sample is found to be around 2 times thicker than other samples deposited with the same duration of 60 minutes. By the time of writing this thesis, no theory was found to elaborate on this phenomenon. It might be ascribed to an operational mistake during the thin film deposition process.

The thicknesses of sample CeSiN-Pure and CeSiN-28 can also be directly determined from the VASE spectrum. Figure 39 shows the comparison between the VASE data of CeSiON-28 and SiON-28. Thicker films always yield more oscillation (peaks and valleys) on the VASE data. So one can compare the thickness of two samples directly from the spectrum.
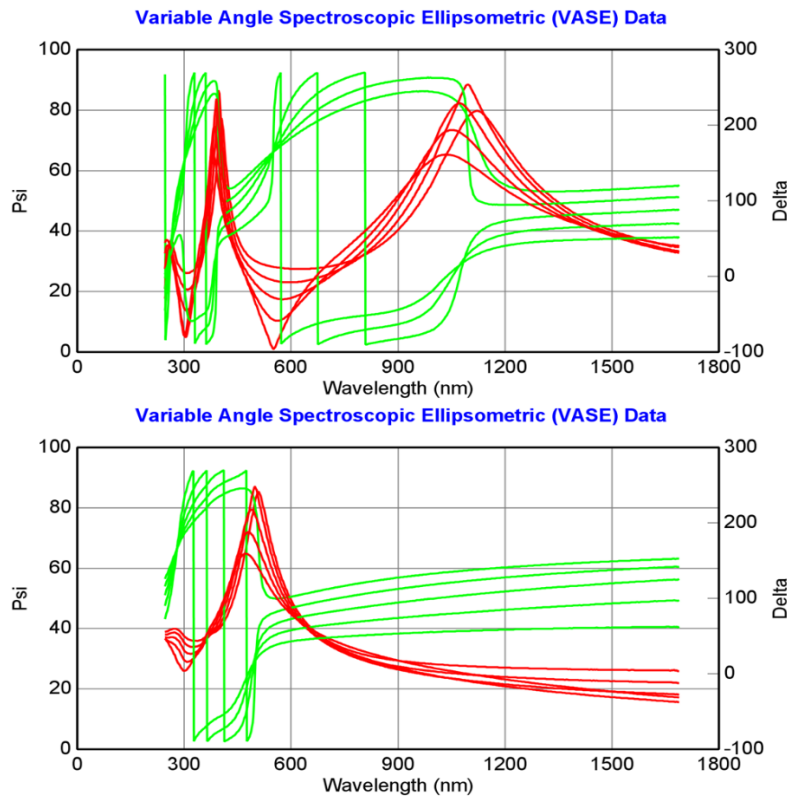
Figure 39. VASE data of CeSiN-28 (top) and SiN-28 (bottom).

For the batch of Ce-doped samples, an average MSE of 5.73 was obtained. More fitting parameters of Ce doped samples can be found in table_3.

Table 3. VASE fitting parameters for Ce doped samples.

Samples	MSE	A	B	C
CeSiO-0	10.238	1.491	0.00628	-3.90E-05
CeSiON-7	4.729	1.479	0.00325	9.38E-05
CeSiON-14	4.453	1.486	0.003	0.000115
CeSiON-21	7.962	1.508	0.00598	-3.44E-05
CeSiN-28	4.212	1.546	0.01828	-0.00095
CeSiN-pure	2.817	1.527	0.01173	-4.61E-05
Average	5.73507	1.50623	0.00809	-0.00014
Std.Dev.	2.78304	0.02586	0.0059	0.0004

The optical constants of both sample batches are shown in Figures 40 and 41. Sometimes the fitting software yields an unphysical result with an ideal MSE, due to the unphysical curve of refractive index versus wavelength. A decrease of the refractive index with increasing wavelength can be observed in both figures, demonstrating the modeling of the VASE experimental data is physically feasible. Therefore, meaningless results generated by the software can be determined by checking the plot of refractive index versus wavelength.

Optical Constants
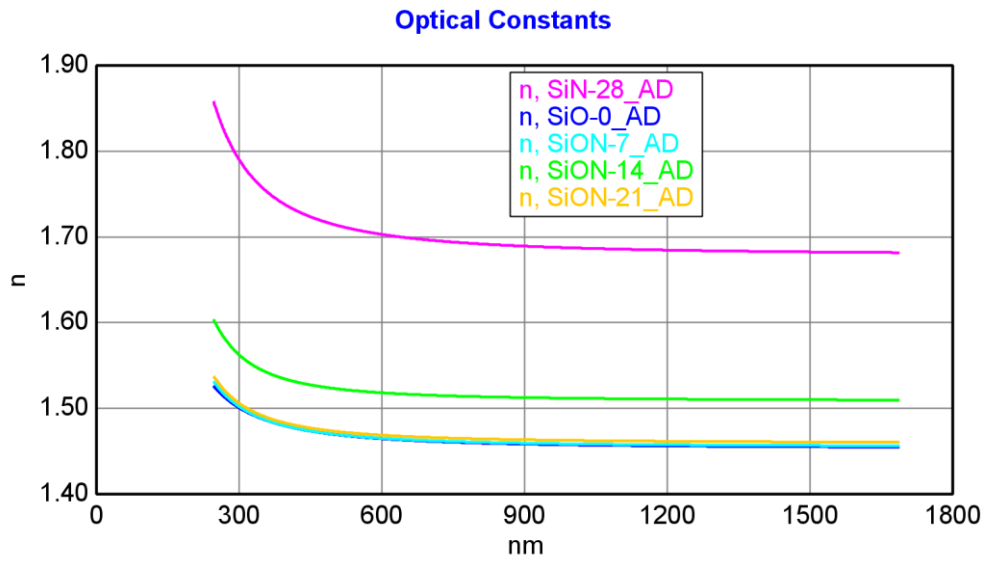
Figure 40. The refractive indexes of reference samples.

Optical Constants
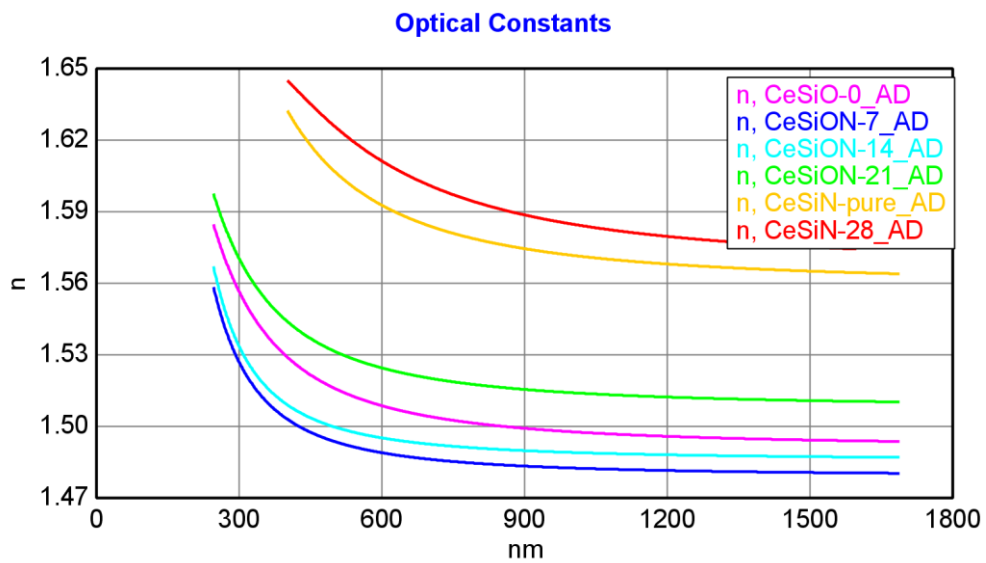
Figure 41. The refractive indexes of Ce doped samples.

It should be mentioned that conventionally, the optical bandgap of the thin film can be calculated using VASE experiment data. However, for the thin

films in this thesis, the bandgaps are estimated to be high (5 – 10 eV). So the VASE spectrum ranging from 300 nm (4.1 eV) to 1700 nm (0.7 eV) is not able to determine the bandgap values.

4.3 Photoluminescence

The investigation of the luminescence properties of Ce-doped samples will be discussed in detail in this section. Photoluminescence spectra were measured with the experimental setup described in Section 3.3, at room temperature and in a dark environment. Visible blue/white PL was observed for all samples with Ce-doping. Great PL enhancements were obtained for all samples subjected to post-deposition annealing at high temperatures ranging from 800 – 1200 °C. Figure 42 shows the blue/white PL emission obtained from annealed sample CeSiON-21 in both daylight and dark condition.
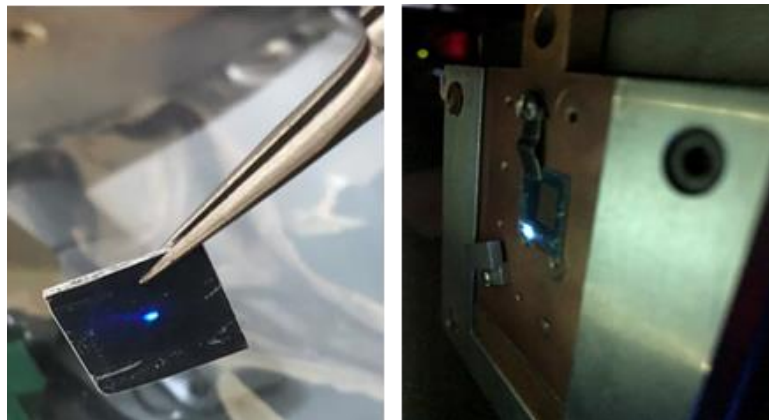
Figure 42. PL of CeSiON-21 annealed at 1200 °C in N_2 and H_2 under daylight and in the dark. Photos are taken by a smartphone camera with 10 Mega Pixels.

Figure 43. PL spectra of the sample set CeSiO-0 annealed at different temperatures.

Figure 43 shows the PL spectra of the sample set CeSiO-0 with and without PDA. The PDA was performed using forming gas (95% nitrogen and 5% hydrogen) for 1 hour. The PL irradiance increases as the annealing temperature increases. Especially for the sample annealed at 1200 °C, the PL irradiance increased dramatically, by more than two orders of magnitude compared to the irradiance of the AD sample. Thus, in this case, annealing conditions with higher annealing temperature yield a higher concentration of Ce-containing clusters. Although wide-band emissions from Ce-based materials have been reported[21,46,47,48,49,50], to the best of the author's knowledge, the

emission spanning the visible range from 400 – 700 nm is reported for the first time in this work. Additionally, the wideband emission does not correspond to any of the Ce 4f energy transitions[51]. It is suggested that the wideband emission originates from defects in the thin films, in the presence of Ce-containing clusters. It is worth mentioning that no emission was obtained from any of the reference samples that do not contain any Ce even when annealed under the same conditions in the same annealing batch. Therefore, we suggest that the Ce-containing clusters in the thin film are functioning as defects and emitting light.

Figure 44 shows the PL spectra of sample set CeSiON-7 with and without PDA. It can be easily found that annealing at 1200 °C in 95 % N_2 and 5 % H_2 (NH) can significantly increase the PL irradiance.
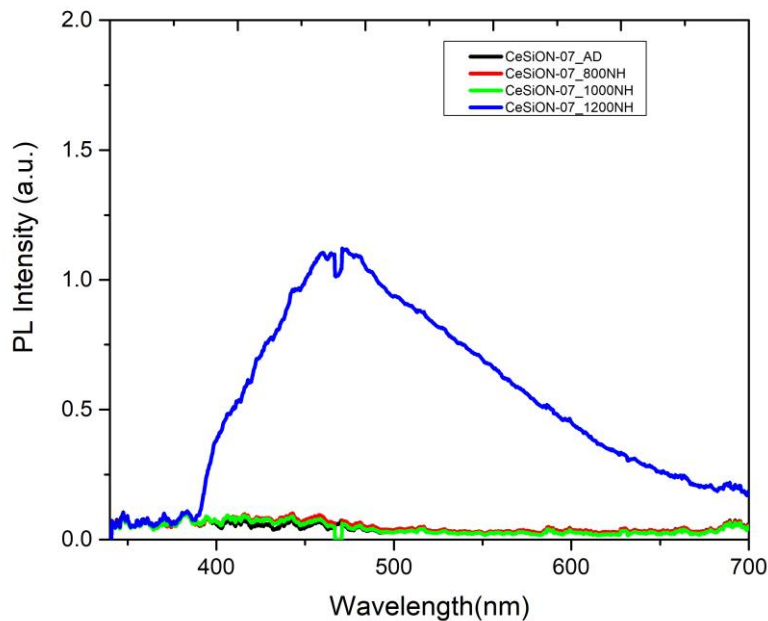
Figure 44. PL spectra of the sample set CeSiON-7 annealed at different temperatures.

Figure 45 shows the PL spectra of sample set CeSiON-14 with and without PDA.

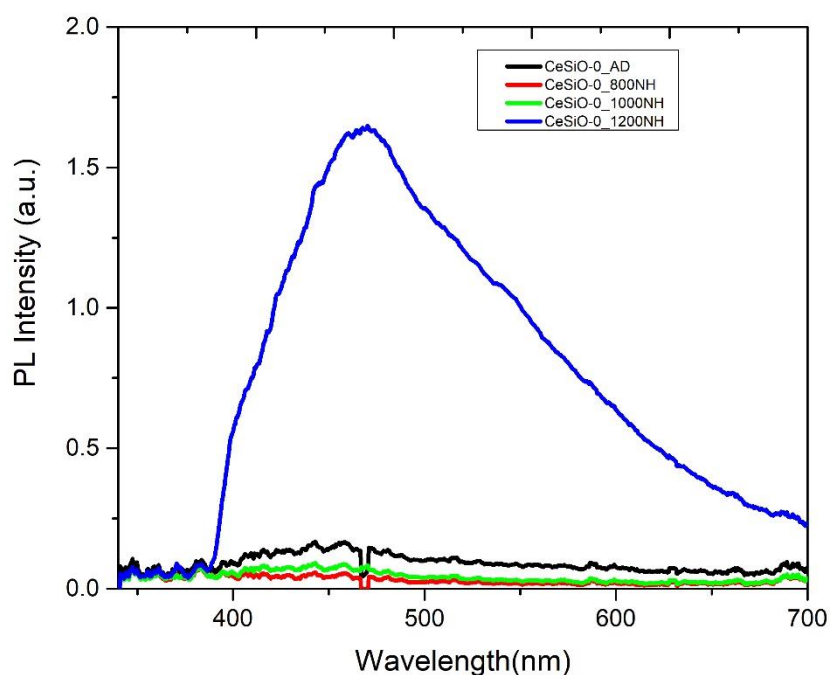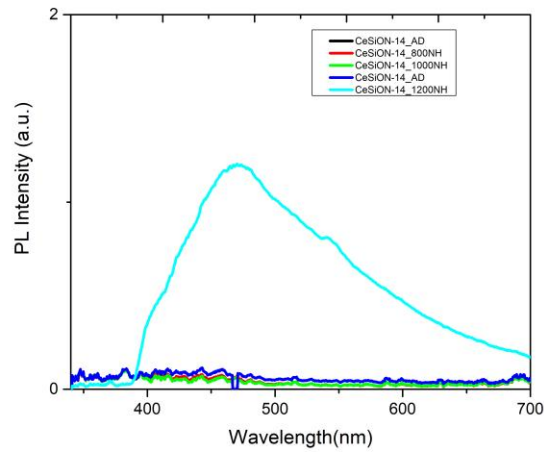*Figure 45. PL spectra of the sample set CeSiON-14 annealed at different temperatures.*

Figure 46 shows the PL spectra of sample set CeSiON-21 with and without PDA.
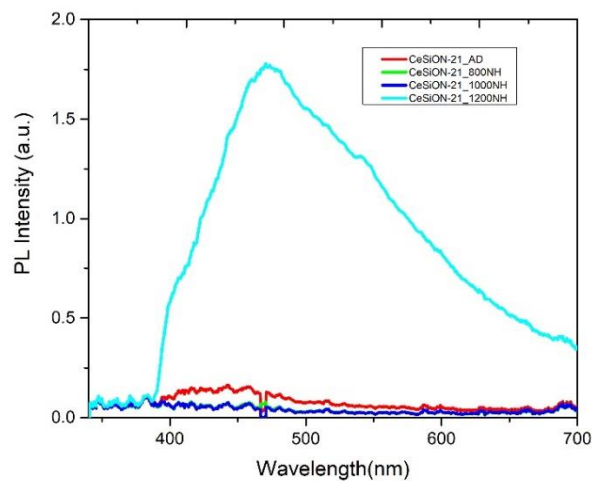
Figure 46. PL spectra of the sample set CeSiON-21 annealed at different temperatures.

Figure 47 shows the PL spectra of sample set CeSiON-28 with and without PDA.
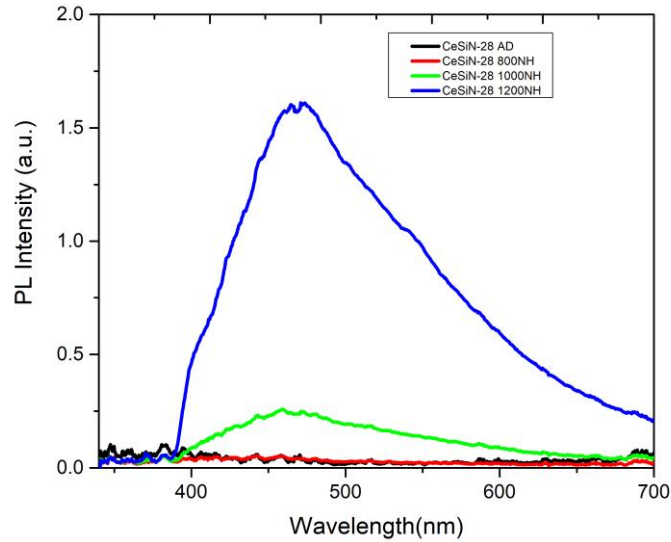
Figure 47. PL spectra of the sample set CeSiN-28 annealed at different temperatures.

Figure 48 shows the PL spectra of sample set CeSiON-pure with and without PDA. A second peak at 550 nm is observed for the sample annealed at 1200 °C. This peak was first considered to be noise or to originate from measurement mistakes, but it still remains after taking multiple scans. However, after repeating the fabrication of this sample, the second peak disappeared. Therefore, the unexpected peak at 540 nm might be from the Terbium (Tb) ions originating from accidental contaminations since both the Tb and Ce metal organic powder cells are connected to the same pipeline leading to the deposition chamber.
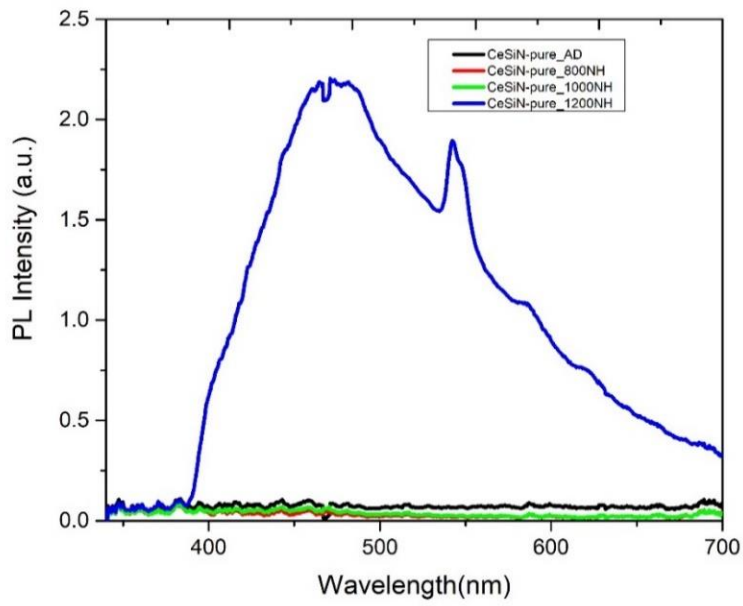
Figure 48. PL spectra of the sample set CeSiN-pure annealed at different temperatures.
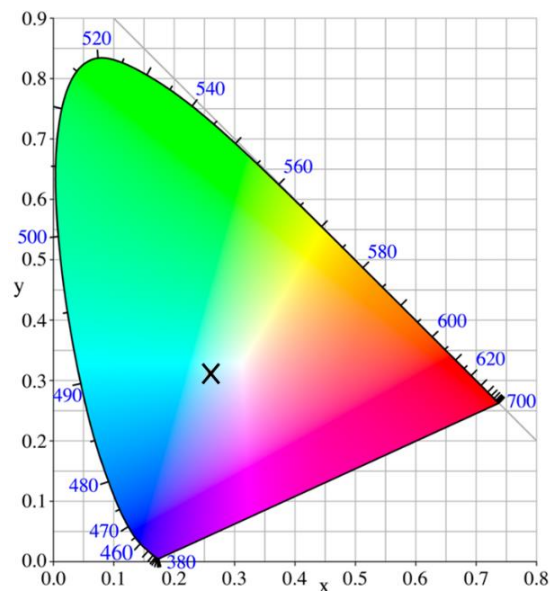
Figure 49. The CIE color coordinate of CeSiON-28 annealed at 1200 °C.

Figure 49 shows the color coordinate (CIE 1931) of sample CeSiON-28 annealed at 1200 °C. The emission is positioned at x = 0.26 and y = 0.31 in the diagram, which is very close to the position of "white" light with coordinates of x = 0.33 and y = 0.33[52]. Figure 50 shows the CIE color coordinates of all Ce-doped samples annealed at 1200 °C in 95 % N_2 and 5 % H_2. Detailed information about the coordinates can be found in Table 5.
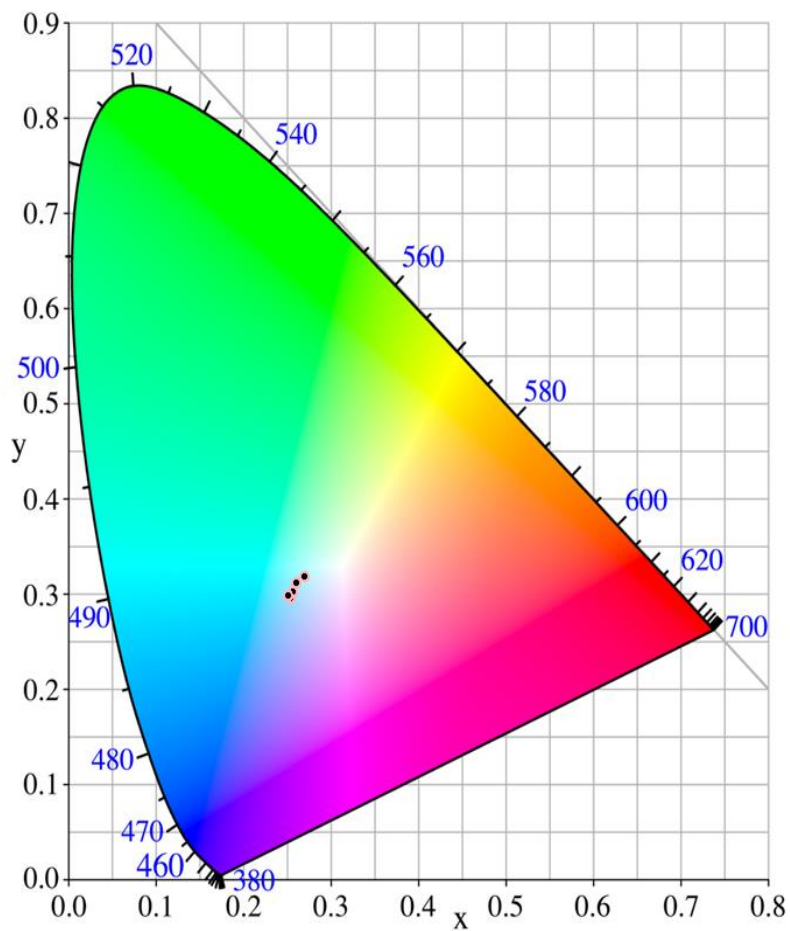
Figure 50. The CIE color coordinates of all Ce-doped samples annealed at 1200 °C in 95 % N_2 and 5 % H_2.

From all the PL spectra above, we found that the irradiance varies with the matrix composition. Thus, it is necessary to investigate the influence of the N content on PL irradiance. Figure 51 shows the peak irradiance and integrated irradiance as functions of the ratio between the N2:Ar partial pressure ($P_{N2:Ar}$) and the total operating pressure in the chamber (P_{total}). For the samples containing similar Ce concentrations, the substitution of oxygen by nitrogen in the host matrix greatly affects the PL irradiance of the samples. As is shown in Figure 51, CeSiN-Pure yields the strongest emission among all samples, while CeSiN-21 shows the most intensive emission among samples deposited with diluted N_2 precursor. Thus, the optimal deposition parameter and the annealing condition of Ce-doped SiO_xN_y is obtained.

Table 4. CIE coordinates for all Ce-doped samples.

Samples	CIEx	CIEy	Peak
CeSiO-0	0.2539	0.2963	470
CeSiON-7	0.2566	0.3019	471
CeSiON-14	0.2558	0.3025	470
CeSiON-21	0.2694	0.3183	470
CeSiN-28	0.2513	0.2993	473
CeSiN-pure	0.2597	0.3125	471
Average	0.25778	0.30513	470.833
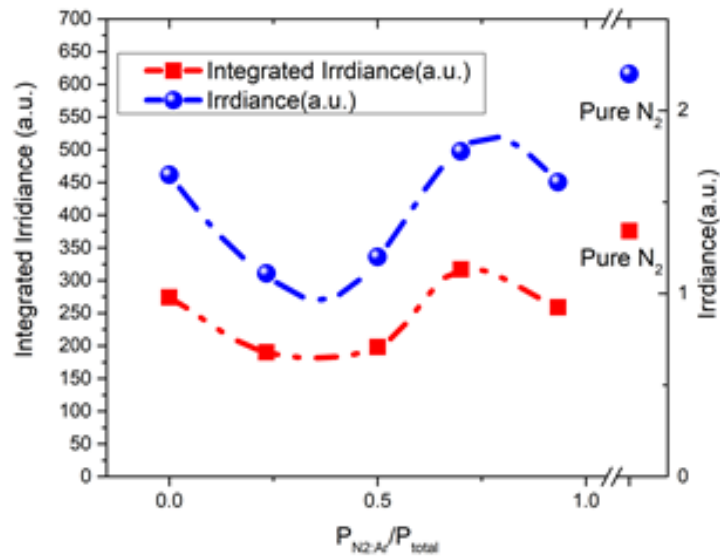
Figure 51. Peak PL irradiance (taken at 470 nm) and PL integrated irradiance as a function of the ratio of the partial N2:Ar pressure and the total deposition pressure in the chamber

Besides, we noticed that after annealing Ce-doped samples at 1200 °C in either NH or N_2, visible contamination was observed in the form of a white coating on the films. Figure 52 shows the surface change of samples after annealing at 1200 °C. Interestingly, this surface coating was not observed on any of the reference samples, indicating that the white coating is related to Ce dopants. This phenomenon was also observed in thin films containing Si-ncs, deposited by a previous group member[30]. However, this phenomenon was not explained thoroughly at that time. Our hypothesis is that both Si-ncs and Ce-containing clusters will introduce defects into the thin film which attract oxygen onto the surface thus forming the white coating.
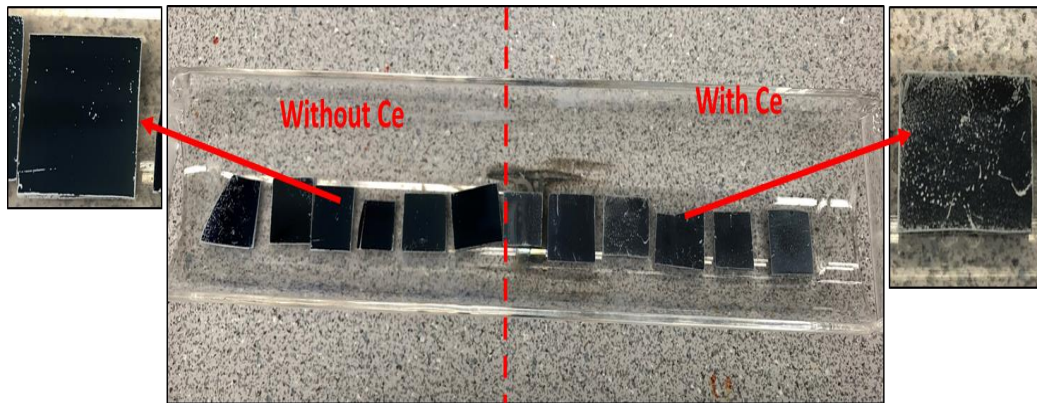
Figure 52. Surface change of samples after annealing at 1200 °C.

In order to investigate the influence of white oxide coating on the PL irradiance of Ce doped samples, we performed hydrogen fluoride (HF) etching on sample CeSiON-21 with different etching durations. Figure 53 shows the integrated PL irradiance of sample CeSiON-21 subjected to annealing at 1200 °C in NH for 1 hour versus the HF etching time. With the increase of HF etching time, the PL irradiance firstly drops and then rises dramatically at an etching time of 120 s. With continuous HF etching, the PL irradiance dropped to the lowest point. The samples get oxygen contamination during the annealing, due to the impurity of the annealing gas. Thus, by etching the surface layer one could potentially improve the PL efficiency. However, HF etching with long duration time could lower the PL irradiance because the emitting layer could be damaged by the HF.
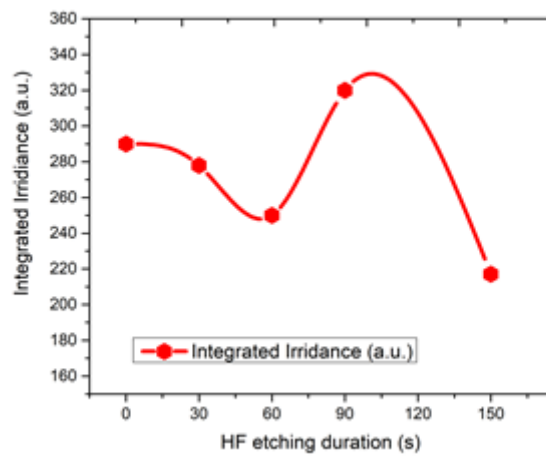
Figure 53. Integrated irradiance of PL versus the HF etching time.
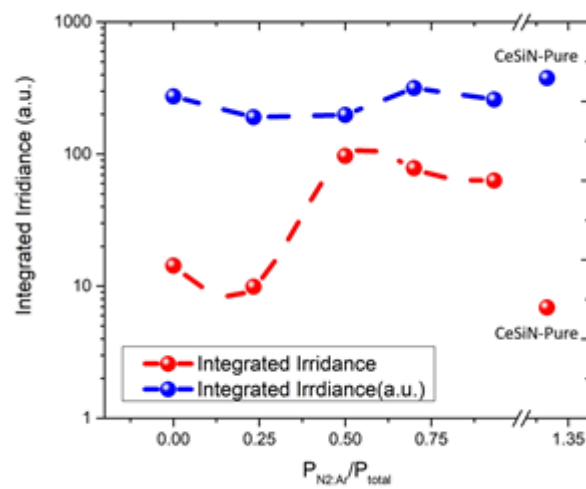
Figure 54.PL irradiance comparison between samples with N2 annealing and NH annealing at 1200 °C

Lastly, the effect of hydrogen passivation on PL irradiance was investigated. Figure 54 shows the integrated irradiance of all Ce-doped samples annealed in a different gas environment at 1200 °C. A significant improvement

of PL intensities of all samples is observed. Notably, for sample CeSiN-Pure, the integrated irradiance of PL is enhanced by 2 orders of magnitude. The enhancement of PL irradiance may be attributed to hydrogen passivation of dangling bonds at the Ce-doped thin film surfaces.

4.4 Charge transport

The charge transport in all of the Ce-doped samples was studied using I-V measurements. The details of the I-V measurement setup are described in Section 3.4. The measurements show excellent charge transport ability of the Ce-doped MIS devices fabricated using RF magnetron sputtering.

Figure 55 shows the I-V curve of sample CeSiO-0 subjected to PDA at 1000 °C NH. A forward I-V sweep was performed with a step of 250 mV/second. The breakdown voltages of devices vary from 40 V to 60 V. Therefore, the I-V plots (Figure 55, Figure 56, and Figure 57) only show voltage sweeps from 0 V to 35 V. A maximum current of around 50 μA was obtained at an applied voltage of 35 V. Considering the thin film thickness and the area of the ITO electrode, the current and voltage correspond to a current density of 100 μA /cm^2 and an electric field of 4.3 x 10^6 MV/cm. Excellent carrier conduction is obtained in this device when compared to a similar MIS device fabricated with an electron beam evaporation system[25], and the current density we achieved is one order of magnitude higher.
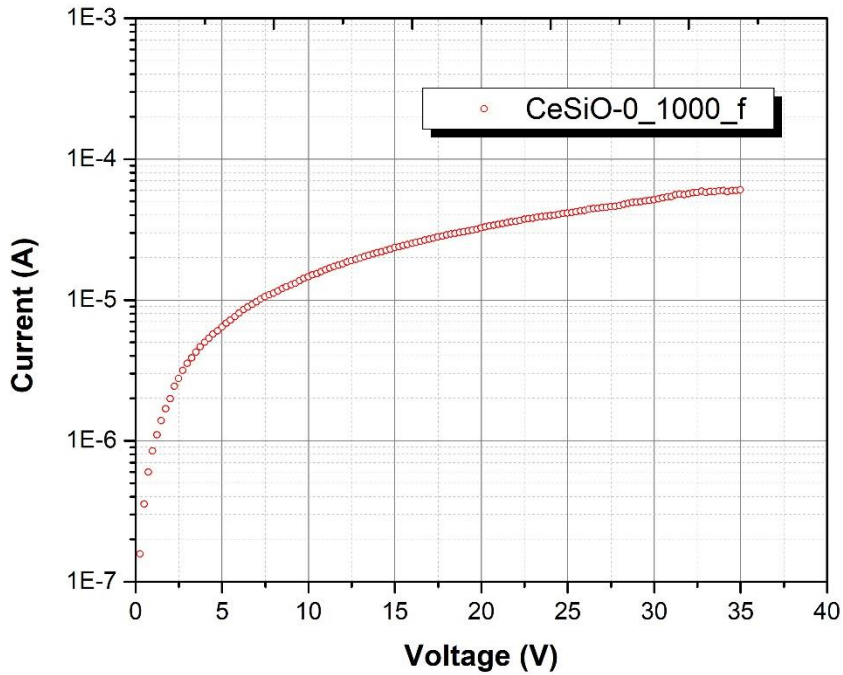
Figure 55.I-V curve of sample CeSiO-0 subjected to PDA at 1000 °C NH.

Despite the fact that all MIS devices are coated with ITO and Al in the same batch and subjected to the sample RTA process, the electrode qualities of the devices vary from device to device, which would cause more uncertainties when investigating the influence of N content on the carrier conduction property. Figure 56 shows the comparison of the I-V curves of three different MIS devices (CeSiON-7, CeSiON-14, and CeSiON-21) with the same PDA condition in a reverse sweep from 0 V to -40 V. The 'r' in the legend denotes the curve is measured in reverse bias. All three MIS devices demonstrated good carrier conduction ability. Besides, the device with more N content demonstrated better

conduction ability. Device CeSiON-21 with the highest N content has better carrier conduction than the other two devices with relatively low N content. This agrees with the fact that introducing more N in the thin film matrix will cause bandgap shrinkage and promote carrier conduction ability of the device.
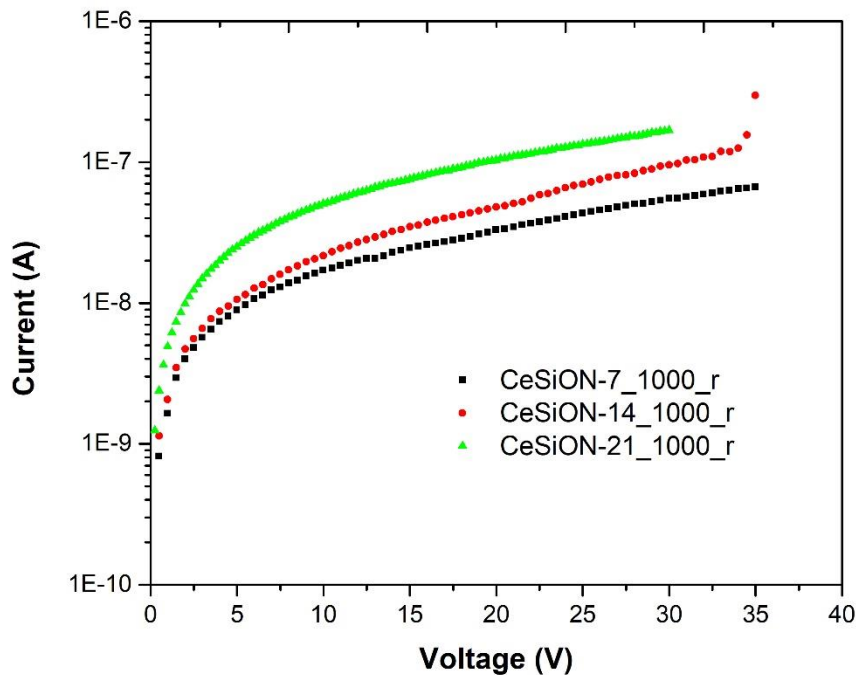
Figure 56. I-V curves with reverse bias of samples CeSiON-7, CeSiON-14, and CeSiON-21 subjected to PDA at 1000 °C NH.

In addition, we also need to investigate which conduction mechanism is playing the main role in the overall carrier conduction process. P-F emission always exists in such devices due to the high concentration of defect sites in the dielectric layer. Figure 57 shows the I-V characteristic of the CeSiO-0 sample. The insert shows $ln(I/V)$ plotted as a function of $V^{1/2}$ which yields a linear curve.

The blue squares are the data points and the red line is the linear fitting. From equation (1.6) we know that for P-F emission the plot of $ln(J/E)$ as a function of $E^{1/2}$ should be linear. The plot of $ln(I/V)$ versus $V^{1/2}$ should reflect the relationship between $ln(J/E)$ and $E^{1/2}$ since the thickness and the area of the electrode of the MIS device are constant. Therefore, we can draw the conclusion that P-F emission is playing a major role in the carrier conduction process.
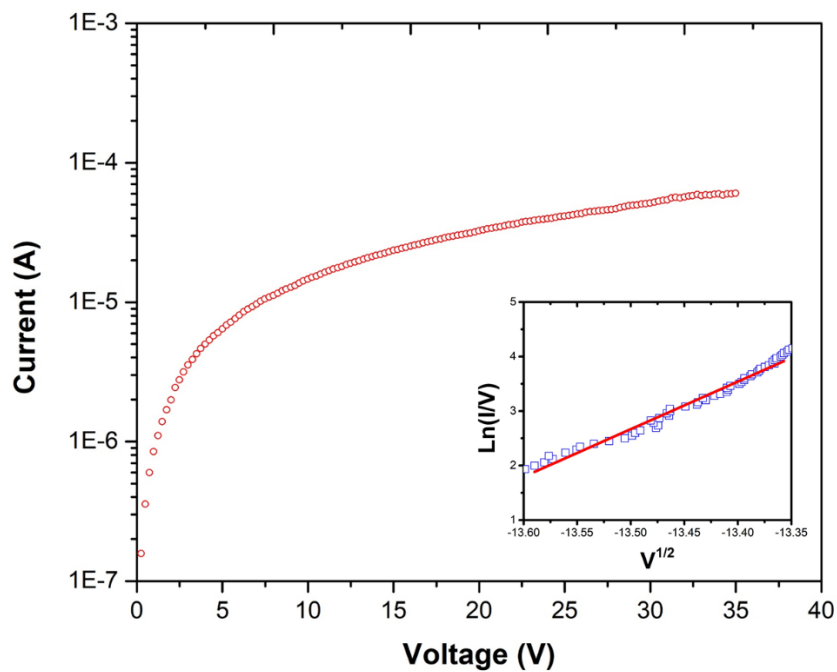
Figure 57.The I-V characteristic of the CeSiO-0 sample. The insert shows ln(I/V) plotted as a function of $V^{1/2}$.

5. Conclusions

Ce doped silicon oxide and oxynitride thin films and their reference samples were deposited using the ECR-PECVD system adapted for in-situ incorporation of rare earths. The thin films were studied in terms of their elemental composition, optical constants, PL properties, and carrier conduction.

Successful in-situ Ce^{3+} doping was achieved with the ECR-PECVD system. By varying the deposition parameters including the flow rates of different gas precursors, thin films with different stoichiometries were obtained. Atomic concentrations of Ce ions ranging from 0.5% to 0.9% were obtained. Besides, reference samples without any Ce doping were also fabricated with the same deposition parameters corresponding to the Ce doped samples, by changing the Ce/Ar gas precursor to an Ar gas precursor.

Elemental compositional analysis was carried out using the RBS technique. Good fittings were obtained for all RBS spectra. The concentrations of Si, O, and Ce fluctuated slightly across all samples (Si at. % 22.3 – 26.5%, O at 48.6 – 57.4 %, Ce 0.5 – 0.9 %). With the increase in the N_2:Ar precursor gas during the deposition, a gradual increase of N concentration is observed from 0 % to 5.2 %. However, undesired oxygen contamination was observed in all samples and a leakage detection should be performed for the deposition system.

The thin film thickness and refractive indexes of all samples were studied using VASE measurements. Good fittings using the Cauchy model were

obtained for all samples with average MSE values of 4.2 for reference samples and 5.7 for Ce doped samples. The thicknesses of the reference samples are around 90 nm, while four of the Ce doped samples have thicknesses of 85 nm and two other samples have thicknesses of 137 and 217 nm. The evolution of the refractive indexes from 1.45 to 1.6 for reference samples and 1.48 to 1.55 for Ce doped samples reflected the increased content of N in the thin films. The plots of optical constant n were used to exclude the meaningless fitting results.

PL properties of Ce doped samples were intensively investigated. PL intensities of Ce doped samples are showing sudden increases after annealing at 1200 °C in both NH and N_2 due to the formation of Ce-containing clusters. The optimized fabrication process for the brightest sample was obtained where the pure nitrogen should be used as a deposition precursor for introducing N to the thin film, and the annealing condition is 1200 °C in NH. Compared to annealing in nitrogen, annealing in NH would further enhance the PL irradiance due to the hydrogen passivation of dangling bonds at the Ce doped thin film surfaces. In addition, the oxide surface's influence on PL irradiance was also studied by etching the oxide surface with HF for different durations. An optimized etching time of 90 is suggested to obtain the highest PL irradiance. HF etching beyond this duration would potentially damage the emission layer thus reducing the PL irradiance.

The electrical properties of the deposited thin films were studied using I-V measurements. Good carrier injection was obtained for most of the samples.

The I-V characteristic of MIS devices vary significantly even though they are coated in the same batch and subjected to RTA at the same time. The highest current density of 100 µA/cm^2 was obtained at an electrical field of 4.3 x 10^6 MV/cm. The main mechanism contributing to the carrier conduction is determined to be Poole–Frenkel emission.

6. Future work

There still is some work necessary to be done in the future in order to develop electrically-driven, silicon-based light emitting devices. This work will be discussed in this section.

6.1 Further material optimization

Although in this work the influence of different amounts of nitrogen precursor gas on the PL irradiance was studied, varying other deposition parameters could also potentially further boost the PL irradiance. These parameters include the total deposition pressure, the microwave power, the temperature of the stage heater, the Ar flow rate for RE doping and the temperature of the metal-organic cell. Besides, post-deposition annealing at a temperature higher than 1200 °C has not been performed in this work due to the temperature limitation of the quartz tube furnace. However, we believe a higher annealing temperature below 1400 °C would enhance the PL irradiance further.

Besides, X-Ray Diffraction (XRD) has been performed for CeSiON-21 sample annealed at 1200 °C in NH. As is shown in Figure 58, no crystallization was observed in this sample. It is suggested that AD samples should be also measured with XRD to see the changes of nanostructures of the sample after annealing.
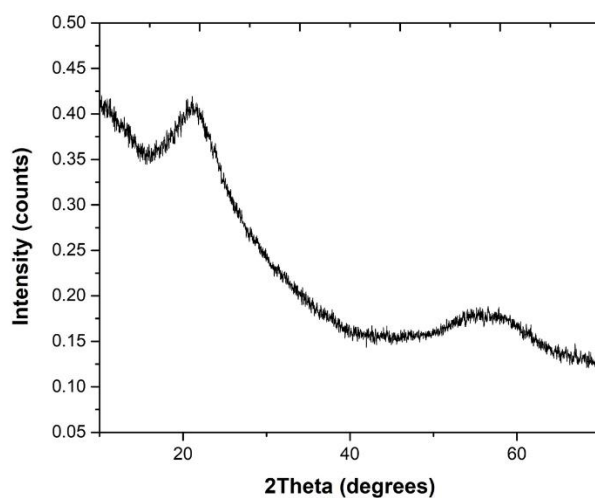
Figure 58. XRD spectra of CeSiON-21 after annealing.

One could also try to determine the content of Ce^{4+} presenting in the thin film. The luminescence of the sample might be enhanced by reducing the content of Ce^{4+} in the sample.

6.2 Quantum efficiency

Quantum efficiency measurements were not completed in this work due to the overlap of the luminescence of the sample and the luminescence of the internal coating of the integrating sphere. A 400 nm long-pass filter was used to block the emitted light from saturating the detector. However, in order to obtain a good measurement of the PL spectrum, a higher integrating time is required due to the lack of sensitivity of the detector connected to the integrating sphere. Therefore, the laser beam at 375 nm would also be amplified and saturate the

detector. The suggestion is to try a different integrating sphere or even try to design a different way to determine the quantum efficiency.

6.3 Red emitter characterization

During the early stage of my depositions, I accidentally deposited a sample with a colorful pattern on the thin film surface which was not observed in other samples deposited using the ECR-PECVD system. The only rare earth element used was terbium (Tb) according to the lab logbook. PL measurements showed visible orange emission for AD samples and strong red emission for a 1200 °C NH annealed sample (shown in figure 59).

Figure 59. Red emission from unknown sample.

This is particularly interesting because it could open a new way to obtain red light-emitting devices based on silicon materials for RGB display. Researchers have been trying to realize red emission through europium (Eu) doping, but no significant process has been made so far.

RBS and VASE measurements were performed on this sample to determine the composition and optical constants. However, irregular spectra were obtained from both RBS and VASE and it is challenging to properly fit those spectra. Figures 60 and 61 show the RBS and VASE measurement data, and it can be observed that these spectra are not like the spectra of 'conventional' samples deposited using the ECR-PECVD system.
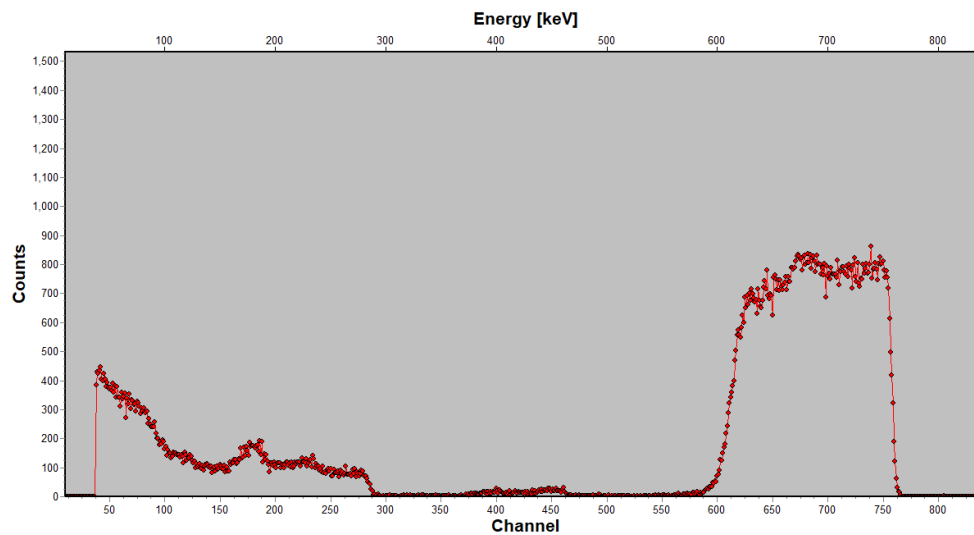
Figure 60. RBS spectrum of the unknown sample.
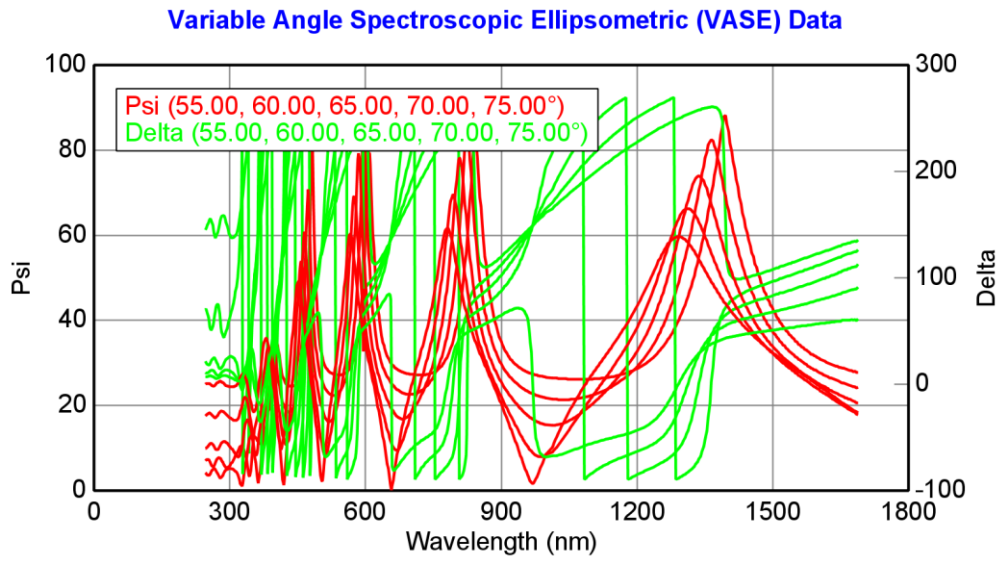
Figure 61. VASE data of the unknown sample.

Therefore, it would be interesting to investigate the unknown sample.

6.4 Device optimization

The large bandgap of silicon oxide and silicon oxynitride make the carrier injection difficult. Although defects in the film would help the carrier conduction, it would also increase the probability of device breakdown[53]. Further increase in the N content in the thin film would decrease the bandgap, which would be beneficial for device fabrication.

Besides, no visible electroluminescence (EL) was observed for the devices. One possible explanation is the lack of transparency of the top ITO electrode as shown in Figure 62. Copper from the sputtering target substrate

might have been sputtered onto the thin film surface, causing the electrode color to turn brown.

Figure 62. Top ITO electrode.

Fabricating devices with higher quality electrodes would be a good attempt to achieve visible EL.

Besides, the packaging of the device should also be considered in order to achieve good reliability and a long life-span.

References

(1)   Kilby, J. S. Miniaturized Electronic Circuits, US Patent 3138743. **1959**.

(2)   Moore, G. E. Cramming More Components onto Integrated Circuits, Reprinted from Electronics, Volume 38, Number 8, April 19, 1965, Pp.114 Ff. *IEEE Solid-State Circuits Soc. Newsl.* **2009**, *11* (3), 33–35. https://doi.org/10.1109/n-ssc.2006.4785860.

(3)   Priolo, F.; Gregorkiewicz, T.; Galli, M.; Krauss, T. F. Silicon Nanostructures for Photonics and Photovoltaics. *Nat. Nanotechnol.* **2014**, *9* (1), 19–32. https://doi.org/10.1038/nnano.2013.271.

(4)   Lim, A. E. J.; Song, J.; Fang, Q.; Li, C.; Tu, X.; Duan, N.; Chen, K. K.; Tern, R. P. C.; Liow, T. Y. Review of Silicon Photonics Foundry Efforts. *IEEE J. Sel. Top. Quantum Electron.* **2014**, *20* (4). https://doi.org/10.1109/JSTQE.2013.2293274.

(5)   Li, J. M.A.Sc. Thesis, Light Emission from Rare Earth-Doped Silicon Oxide Thin Films Deposited by ECR-PECVD. **2008**.

(6)   Pavesi, L. Will Silicon Be the Photonic Material of the Third Millenium? *J. Phys. Condens. Matter* **2003**, *15* (26). https://doi.org/10.1088/0953-8984/15/26/201.

(7)   Green, M. A.; Zhao, J.; Wang, A.; Reece, P. J.; Gal, M. Ef ® Cient Silicon Light-Emitting Diodes. **2001**, *412* (August), 805–808.

(8)   Zacharias, M.; Heitmann, J.; Scholz, R.; Kahler, U.; Schmidt, M.; Bläsing, J. Size-Controlled Highly Luminescent Silicon Nanocrystals: A SiO/SiO 2 Superlattice Approach. *Appl. Phys. Lett.* **2002**, *80* (4), 661–663. https://doi.org/10.1063/1.1433906.

(9)   Kital, A. *Principles of Solar Cells, LED's and Diodes*; Wiley, 2011.

(10)   Sumanth Kumar, D.; Jai Kumar, B.; Mahesh, H. M. *Quantum Nanostructures (QDs): An Overview*; Elsevier Ltd., 2018. https://doi.org/10.1016/b978-0-08-101975-7.00003-8.

(11)   Shimizu-Iwayama, T.; Kurumado, N.; Hole, D. E.; Townsend, P. D. Optical Properties of Silicon Nanoclusters Fabricated by Ion Implantation. *J. Appl. Phys.* **1998**, *83* (11), 6018–6022. https://doi.org/10.1063/1.367469.

(12)   Hayashi, S.; Yamamoto, K. Optical Properties of Si-Rich SiO2 Films in Relation with Embedded Si Mesoscopic Particles. *J. Lumin.* **1996**, *70* (1-6 SPEC. ISS.), 352–363. https://doi.org/10.1016/0022-2313(96)00070-1.

(13)   Henini, M. Molecular Beam Epitaxy. *Mol. Beam Ep.* **2013**, *500*, 189–217. https://doi.org/10.1016/C2010-0-68986-3.

(14)   Kahler, U.; Hofmeister, H. Size Evolution and Photoluminescence of Silicon Nanocrystallites in Evaporated SiOx Thin Films upon Thermal Processing. *Appl. Phys. A Mater. Sci. Process.* **2002**, *74* (1), 13–17. https://doi.org/10.1007/s003390100993.

(15)   Kenyon, A. J. *Recent Developments in Rare-Earth Doped Materials for Optoelectronics*; 2002; Vol. 26. https://doi.org/10.1016/S0079-6727(02)00014-9.

(16)   Miniscalco, W. J. Erbium-Doped Glasses for Fiber Amplifiers At. **1991**, *9* (2).

(17)   Li, J.; Zalloum, O.; Roschuk, T.; Heng, C.; Wojcik, J.; Mascher, P. The Formation of Light Emitting Cerium Silicates in Cerium-Doped Silicon Oxides. *Appl. Phys. Lett.* **2009**, *94* (1), 3–6. https://doi.org/10.1063/1.3067871.

(18)   Choi, W. C.; Lee, H. N.; Kim, E. K.; Kim, Y.; Park, C. Y.; Kim, H. S.; Lee, J. Y. Violet/Blue Light-Emitting Cerium Silicates. *Appl. Phys. Lett.* **1999**, *75* (16), 2389–2391. https://doi.org/10.1063/1.125023.

(19)   Psuja, P.; Hreniak, D.; Strek, W. Rare-Earth Doped Nanocrystalline Phosphors for Field Emission Displays. *J. Nanomater.* **2007**, *2007*. https://doi.org/10.1155/2007/81350.

(20)   Science Photo Library's https://www.sciencephoto.com/media/553920/view/cerium-atomic-structure.

(21)   Reisfeld, R.; Minti, H.; Patra, A.; Ganguli, D.; Gaft, M. Spectroscopic Properties of Cerium in Glasses and Their Comparison with Crystals. *Spectrochim. Acta - Part A Mol. Biomol. Spectrosc.* **1998**, *54* (13), 2143–

2150. https://doi.org/10.1016/S1386-1425(98)00131-0.

(22)   Xu, G. Q.; Zheng, Z. X.; Tang, W. M.; Wu, Y. C. Luminescence Property of Ce3+-Doped Silica Decorated with S2- and Cl- Anions. *J. Lumin.* **2007**, *126* (2), 475–480. https://doi.org/10.1016/j.jlumin.2006.09.010.

(23)   Fang, Z.; Cao, R.; Zhang, F.; Ma, Z.; Dong, G.; Qiu, J. Efficient Spectral Conversion from Visible to Near-Infrared in Transparent Glass Ceramics Containing Ce3+-Yb3+ Codoped Y 3Al5O12 Nanocrystals. *J. Mater. Chem. C* **2014**, *2* (12), 2204–2211. https://doi.org/10.1039/c3tc32231a.

(24)   Robert, P.; Wilson, J.; Khatami, Z.; Dabkowski, R.; Mascher, P. XANES and XEOL Investigation of Cerium and Terbium Co-Doped Silicon Oxide Films. **2015**, No. April 2012. https://doi.org/10.1149/1.3700408.

(25)   Ramirez, J. Rare Earth-Doped Silicon-Based Light Emitting Devices : Towards New Integrated Photonic Building Blocks, 2015. https://doi.org/10.1189/jlb.4MR0316-108R.

(26)   Chi., K. K. *Dielectric Phenomena in Solids.*; Elsevier, 2004.

(27)   Min Xie, Dongsheng Li, Feng Wang, D. Y. Luminescence Properties of Silicon-Rich Silicon Nitride Films and Light Emitting Transactions, E C S Society, The ElectrochemicalDevices; Transactions, E C S Society, The Electrochemical, 2011; Vol. 35, pp 3–19.

(28)   Chiu, F. C. A Review on Conduction Mechanisms in Dielectric Films. *Adv. Mater. Sci. Eng.* **2014**, *2014*. https://doi.org/10.1155/2014/578168.

M.A.Sc. Thesis – Y. Gao; McMaster University – Engineering Physics.

(29) J. M. Ramírez, J. Wojcik, Y. Berencén, P. Mascher, B.; Garrido, B. On the Photoluminescence of As-Deposited Tb-Doped Silicon Oxides and Oxynitrides Fabricated by ECR-PECVD; Proc. SPIE 9133,Silicon Photonics and Photonic Integrated Circuits IV, 2014; Vol. 913309. https://doi.org/10.1117/12.2052571.

(30) Sacks, J. M.A.Sc. Thesis, Spectral Engineering via Silicon Nanocrystals Grown by Pecvd, McMaster University, 2012.

(31) Rebohle, Lars, and W. S. *Rare-Earth Implanted MOS Devices for Silicon Photonics: Microstructural, Electrical and Optoelectronic Properties.*; Springer Science & Business Media, 2010.

(32) Blakie, D. E.; Zalloum, O. H. Y.; Wojcik, J.; Irving, E. J.; Knights, A. P.; Mascher, P. Coupled Luminescence Centres in Erbium-Doped Silicon Rich Silicon Oxide Thin Films. *Photonics North 2006* **2006**, *6343*, 63433S. https://doi.org/10.1117/12.708049.

(33) Dabkowski, R. P. Installation of a New Electron Cyclotron Plasma Enhanced Chemical Vapour Deposition (ECR- PECVD) Reactor and a Preliminary Study of Thin Film Depositions. **2012**.

(34) Semicore http://www.semicore.com/news/92-what-is-rf-sputtering.

(35) LibreTexts libraries https://chem.libretexts.org/Bookshelves/Analytical_Chemistry/Book%3 A_Physical_Methods_in_Chemistry_and_Nano_Science_(Barron)/01%

M.A.Sc. Thesis – Y. Gao; McMaster University – Engineering Physics.

3A_Elemental_Analysis/1.15%3A_Rutherford_Backscattering_of_Thin _Films.

(36)   Ager, F. J.; Respaldiza, M. A.; Botella, J.; Soares, J. C.; Da Silva, M. F.; Benítez, J. J.; Odriozola, J. A. Rutherford Backscattering Spectrometry (RBS) Characterization of Oxide Scale Formed on (AISI-304) Steel after Surface Deposition of Lanthanum. *Acta Mater.* **1996**, *44* (2), 675–681. https://doi.org/10.1016/1359-6454(95)00193-X.

(37)   Mayer, M.; Mayer, M. SIMNRA User ' s Guide. *Book* **1997**.

(38)   Ziegler, J. F. *The Stopping and Ranges of Ions in Matter.*; Elsevier, 2013.

(39)   J. A. Woollam Co https://www.jawoollam.com/.

(40)   Jenkins, Francis A., and H. E. W. *Fundamentals of Optics*; Tata McGraw-Hill Education, 1937.

(41)   J. Hale and B. Johs. *"CompleteEASE^{TM} Data Analysis Manual";* 2011.

(42)   Ocean Optics. *OOIIrrad Irradiance Software Manual*; 1999.

(43)   Zalloum, O. H. Y.; Flynn, M.; Roschuk, T.; Wojcik, J.; Irving, E.; Mascher, P. Laser Photoluminescence Spectrometer Based on Charge-Coupled Device Detection for Silicon-Based Photonics. *Rev. Sci. Instrum.* **2006**, *77* (2), 1–8. https://doi.org/10.1063/1.2173030.

(44)   Wilson, P. PhD Thesis, Study of Luminescent Silicon-Rich Silicon Nitride and Cerium and Terbium Doped Silicon Oxide Thin Films. **2012**.

(45)   Chen, Z.; Sana, P.; Salami, J.; Rohatgi, A. A Novel and Effective PECVD SiO2/SiN Antireflection Coating for Si Solar Cells. *IEEE Trans. Electron Devices* **1993**, *40* (6), 1161–1165. https://doi.org/10.1109/16.214744.

(46)   Chiba, A.; Tanaka, S.; Inami, W.; Sugita, A.; Takada, K.; Kawata, Y. Amorphous Silicon Nitride Thin Films Implanted with Cerium Ions for Cathodoluminescent Light Source. *Opt. Mater. (Amst).* **2013**, *35* (11), 1887–1889. https://doi.org/10.1016/j.optmat.2013.02.018.

(47)   Lin, G. R.; Pai, Y. H.; Lin, C. T.; Chen, C. C. Comparison on the Electroluminescence of Si-Rich SiNx and SiOx Based Light-Emitting Diodes. *Appl. Phys. Lett.* **2010**, *96* (26), 130–133. https://doi.org/10.1063/1.3459144.

(48)   Sun, J. M.; Prucnal, S.; Skorupa, W.; Helm, M.; Rebohle, L.; Gebel, T. Increase of Blue Electroluminescence from Ce-Doped SiO2 Layers through Sensitization by Gd3+ Ions. *Appl. Phys. Lett.* **2006**, *89* (9), 2004–2007. https://doi.org/10.1063/1.2338892.

(49)   Li, Y. Q.; Hirosaki, N.; Xie, R. J.; Takeda, T.; Mitomo, M. Photoluminescence Properties of Rare Earth Doped α-Si3N4. *J. Lumin.* **2010**, *130* (7), 1147–1153. https://doi.org/10.1016/j.jlumin.2010.02.012.

(50)   LIU, R. S. Tunable Blue-Green Color Emission and Energy Transfer of Ca. *J. Phys. Chem. C* **2012**, *116* (29), 15604–15609.

(51)   Li, J.; Zalloum, O.; Roschuk, T.; Heng, C.; Wojcik, J.; Mascher, P. The

Formation of Light Emitting Cerium Silicates in Cerium-Doped Silicon Oxides. *Appl. Phys. Lett.* **2009**, *94* (1), 5–8. https://doi.org/10.1063/1.3067871.

(52)   Park, N. M.; Kim, T. S.; Park, S. J. Band Gap Engineering of Amorphous Silicon Quantum Dots for Light-Emitting Diodes. *Appl. Phys. Lett.* **2001**, *78* (17), 2575–2577. https://doi.org/10.1063/1.1367277.

(53)   Helm, M.; Sun, J. M.; Potfajova, J.; Dekorsy, T.; Schmidt, B.; Skorupa, W. Efficient Silicon Based Light Emitters. *Microelectronics J.* **2005**, *36* (11), 957–962. https://doi.org/10.1016/j.mejo.2005.04.002.